Computational Mechanics 21 (1998) 172–188 © Springer-Verlag 1998

Finite element computation of unsteady viscous transonic flows past stationary airfoils

S. Mittal

Abstract Results are presented for computations of unsteady viscous transonic flows past a stationary *NACA*0012 airfoil at various angles of attack. The Reynolds number, based on the chord-length of the airfoil, is 10,000 and the Mach number is 0.85. Stabilized finite-element formulations are employed to solve the compressible Navier-Stokes equations. The equation systems, resulting from the discretization, are solved iteratively by using the preconditioned GMRES technique. Time integration of the governing equations is carried out for large values of the non-dimensional time to understand the unsteady dynamics and long-term behavior of the flows. The results show interesting flow patterns and a complex interaction between the boundary/shear layers, shock/expansion waves and the lateral boundaries of the computational domain. For transonic flow past an airfoil at various angles of attack in a narrow channel/wind-tunnel one can observe solutions that are qualitatively different from each other. At low angles of attack an unsteady wake is observed. At moderate angles of attack the interaction between the shock system and the lateral walls becomes significant and the temporal activity in the wake decreases and eventually disappears. At high angles of attack a reflection shock is formed. Hysteresis is observed at an angle of attack 8°. For the flow in a domain with the lateral boundaries located far away, the unsteadiness in the flow increases with an increase in the angle of attack. Computations for a Mach 2, Re 106 flow past an airfoil at 10° angle of attack compare well with numerical and experimental results from other researchers

1 Introduction

Accurate computation of viscous transonic flows past wings and airfoils is vital to the design of advanced airplanes. There have been numerous efforts in the past to compute steady inviscid transonic flows (Hughes and Tezduyar 1984; Bristeau et al. 1985; Lohner et al. 1985; Le Beau and Tezduyar 1991; Tezduyar and Hughes 1983; Peraire et al. 1993; Johan 1992). Viscous flow computations for steady transonic flows have also been carried out by various researchers (Bristeau et al. 1988; Muller and Rizzi 1988; Jameson and Schmidt 1985; Boivin and Fortin 1993; Aliabadi and Tezduyar 1995). Some of these studies involve computations of flow past an entire airplane. However, fewer studies have been conducted for unsteady, transonic, viscous flows (Bristeau et al. 1988; Boivin and Fortin 1993; Sarkis et al. 1996; Mittal 1998). It is interesting to note that unsteady computations for incompressible flows past wings and airfoils are carried out quite routinely (Mittal and Tezduyar 1992, 1994, 1995). Some other unsteady flow results can be found in articles by Karanth et al. [18] and Tezduyar et al. (1996). Unsteady compressible flows involving airfoils at low Mach numbers, in the subsonic regime, have also been computed by various researchers, for example, by Dortmann (1988) and Aliabadi and Tezduyar (1993).

In this article, results are presented for the computation of unsteady viscous transonic flows past airfoils at various angles of attack. Such flows are associated with complex unsteady interactions between the boundary/shear layers and shock/expansion waves and, in the numerical simulations, care must be taken to adequately resolve the associated temporal and spatial structures. Another issue that deserves utmost attention is the one of imposing the right set of boundary conditions for the compressible Navier-Stokes equations. The interested reader is referred to the work by Oliger and Sundstrom (1978) and Gustafssons and Sundstrom (1978). In the present work, computations for Mach 0.85 and Re 10,000 flow past a *NACA0012* airfoil are carried out for two locations of the lateral boundaries. When the lateral boundaries are located at 12 chord-lengths, each, from the airfoil, there is no interaction between the flow and the two boundaries. It is observed that the lambda shock, formed near the airfoil surface, becomes stronger as the angle of attack of the airfoil increases. The unsteadiness in the wake also increases as the angle of incidence of the airfoil, with the free-stream flow, increases. The situation changes when the lateral boundaries are brought closer to the airfoil. Computations have been carried out for the case when the lateral boundaries are located at 4.25 chord-lengths, each, from the airfoil. This case is quite similar to the flow past an airfoil in a narrow channel. The channel walls are, however, assumed to allow for the slip-flow. Except at

Communicated by S. N. Atluri, 20 October 1997

S. Mittal
Department of Aerospace Engineering,
Indian Institute of Technology, Kanpur,
UP 208 016, India

Partial support for this work has come from the Aeronautical Development Agency, India under the project number ADA-AE-95204. The author would like to thank Prof. N. L. Arora, Department of Aerospace Engineering, IIT Kanpur, for providing access to his computational resources.

small angles of attack (α) there is a significant interaction between the flow and channel walls. Beyond a certain angle of attack, increasing α leads to a decrease in the unsteadiness in the wake of the flow, till at $\alpha = 8^\circ$ the flow becomes steady. Beyond $\alpha = 8^\circ$ the flow remains steady while the shock-structure goes through a qualitative change. At $\alpha = 10^\circ$ a set of shocks reflected from the lateral boundaries can be observed in the solution. When this solution is used as an initial condition to compute the flow at $\alpha = 8^\circ$, by slowly ramping the angle of attack, a steady-state flow is achieved again. However, the shock-structure of this flow is quite different than the one obtained earlier. This suggests that there is hysteresis in the flow close to $\alpha = 8^\circ$, i.e., the solution depends on the initial conditions. When the angle of attack is decreased further, the flow becomes unsteady again and is independent of the initial conditions. It is interesting to note that Bristeau et al. (1985) also reported the existence of multiple solutions for their computation of steady inviscid potential transonic flows past a *NACA*0012 airfoil at various angles of attack. It must, however, be pointed out that the reasons for the presence of multiple solutions reported by Bristeau et al. (1985) and for the present computations are quite different. The multiple solutions in the present computations are a result of strong interaction of the flow and lateral boundaries. In the case of inviscid potential flows the Kutta-Joukowsky condition needs to be satisfied explicitly for airfoils with sharp trailing edge. This along with other conditions are not sufficient to ensure uniqueness of the solution as observed by Bristeau et al. (1985).

The organization of the remaining article is as follows. First, the governing equations for the flow are reviewed in Sect. 2. The equations are written in the conservation law form. The stabilized variational formation of these equations in terms of the conservation variables is presented in Sect. 3. The SUPG (Streamline-Upwind/Petrov-Galerkin) stabilization technique is employed to stabilize the computations against spurious numerical oscillations due to advection dominated flows. The SUPG technique was first introduced by Hughes and Brooks (1979) for the advection-diffusion equation and for incompressible flows. It was introduced in the context of inviscid compressible flows by Tezduyar and Hughes (1983, 1982) and Hughes and Tezduyar (1984). In addition to the SUPG stabilizations, a shock-capturing term is added to the formulation to provide stability of the computations in the presence of discontinuities and large gradients in the flow. This idea, in the context of conservation variables, was demonstrated by Le Beau and Tezduyar (1991). In Sect. 4 numerical results for computations of flows past airfoils at various angles of attack are presented and discussed. Finally, a few concluding remarks are made in Sect. 5.

2
The governing equations

Let $\Omega \subset \mathbb{R}^{n_{sd}}$ and $(0, T)$ be the spatial and temporal domains respectively, where n_{sd} is the number of space dimensions, and let Γ denote the boundary of Ω. The spatial and temporal coordinates are denoted by $\mathbf{x}$ and t. The Navier-Stokes equations governing the fluid flow, in conservation form, are

$$\frac{\partial \rho}{\partial t} + \nabla \cdot (\rho \mathbf{u}) = 0 \quad \text{on } \Omega \text{ for } (0, T) \ , \tag{1}$$

$$\frac{\partial (\rho \mathbf{u})}{\partial t} + \nabla \cdot (\rho \mathbf{u}\mathbf{u}) + \nabla p - \nabla \cdot \mathbf{T} = \mathbf{0} \text{ on } \Omega \text{ for } (0,T) \ , \tag{2}$$

$$\frac{\partial (\rho e)}{\partial t} + \nabla \cdot (\rho e \mathbf{u}) + \nabla \cdot (p\mathbf{u}) - \nabla \cdot (\mathbf{T}\mathbf{u}) + \nabla \mathbf{q} = 0 \quad \text{on } \Omega \text{ for } (0, T) \ . \tag{3}$$

Here ρ, $\mathbf{u}$, p, $\mathbf{T}$, e, and $\mathbf{q}$ are the density, velocity, pressure, viscous stress tensor, the total energy per unit mass, and the heat flux vector, respectively. The viscous stress tensor is defined as

$$\mathbf{T} = \mu\big((\nabla \mathbf{u}) + (\nabla \mathbf{u})^{\mathrm{T}}\big) + \lambda (\nabla \cdot \mathbf{u})\mathbf{I} \ . \tag{4}$$

where μ and λ are the viscosity coefficients. It is assumed that μ and λ are related by

$$\lambda = -\tfrac{2}{3}\mu \ . \tag{5}$$

Pressure is related to the other variables via the equation of state. For ideal gases, the equation of state assumes the special form

$$p = (\gamma - 1)\rho i \ , \tag{6}$$

where γ is the ratio of specific heats and i is the internal energy per unit mass that is related to the total energy per unit mass and velocity as

$$i = e - \tfrac{1}{2}\|\mathbf{u}\|^2 \ . \tag{7}$$

The heat flux vector is defined as

$$\mathbf{q} = -\kappa \nabla \theta \ , \tag{8}$$

where κ is the heat conductivity and θ is the temperature. The temperature is related to the internal energy by the following relation

$$\theta = \frac{\mathrm{R}}{\gamma - 1} i \ , \tag{9}$$

where R is the ideal gas constant. Prandtl number (Pr), assumed to be specified, relates the heat conductivity to the fluid viscosity according to the following relation

$$\kappa = \frac{\gamma \mathrm{R} \mu}{(\gamma - 1)\mathrm{Pr}} \ . \tag{10}$$

The compressible Navier-Stokes equations (1), (2), and (3) can be written in the conservation variables

$$\frac{\partial \mathbf{U}}{\partial t} + \frac{\partial \mathbf{F}_i}{\partial x_i} - \frac{\partial \mathbf{E}_i}{\partial x_i} = \mathbf{0} \quad \text{on } \Omega \text{ for } (0, T) \ , \tag{11}$$

where $\mathbf{U} = (\rho, \rho u_1, \rho u_2, \rho e)$, is the vector of conservation variables, and $\mathbf{F}_i$ and $\mathbf{E}_i$ are, respectively, the Euler and viscous flux vectors defined as

$$\mathbf{F}_i = \begin{pmatrix} u_i \rho \\ u_i \rho u_1 + \delta_{i1} p \\ u_i \rho u_2 + \delta_{i2} p \\ u_i (\rho e + p) \end{pmatrix} \ , \tag{12}$$

$$\mathbf{E}_i = \begin{pmatrix} 0 \\ \tau_{i1} \\ \tau_{i2} \\ -q_i + \tau_{ik} u_k \end{pmatrix} \quad . \tag{13}$$

Here u_i, q_i, and τ_{ik} are the components of the velocity, heat flux, and viscous stress tensor, respectively. In the quasi-linear form Eq. (11) is written as

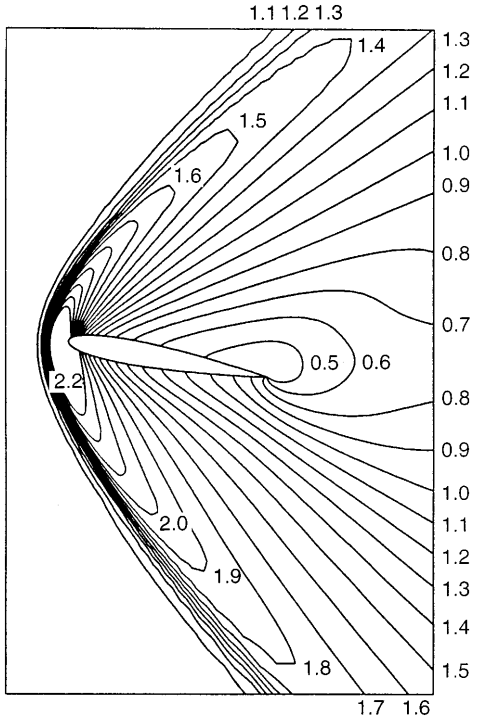

Fig. 1. $M = 2.0$, Re $= 106$, $\alpha = 10^\circ$ flow past a *NACA*0012 airfoil: density field for the steady-state solution from the present computations

$$\frac{\partial \mathbf{U}}{\partial t} + \mathbf{A}_i \frac{\partial \mathbf{U}}{\partial x_i} - \frac{\partial}{\partial x_i}\left(\mathbf{K}_{ij} \frac{\partial \mathbf{U}}{\partial x_j}\right) = \mathbf{0} \quad \text{on } \Omega \text{ for } (0, T) \ , \tag{14}$$

where

$$\mathbf{A}_i = \frac{\partial \mathbf{F}_i}{\partial \mathbf{U}} \ , \tag{15}$$

is the Euler Jacobian Matrix, and $\mathbf{K}_{ij}$ is the diffusivity matrix satisfying

$$\mathbf{K}_{ij} \frac{\partial \mathbf{U}}{\partial x_j} = \mathbf{E}_i \ . \tag{16}$$

Corresponding to Eq. (14), the following boundary and initial conditions are chosen

$$\mathbf{U} = \mathbf{g} \quad \text{on } \Gamma_g \text{ for } (0, T) \ , \tag{17}$$

$$\mathbf{n} \cdot \mathbf{E} = \mathbf{h} \quad \text{on } \Gamma_h \text{ for } (0, T) \ , \tag{18}$$

$$\mathbf{U}(\mathbf{x}, 0) = \mathbf{U}_0 \quad \text{on } \Omega_0 \ . \tag{19}$$

3 Finite element formulation

Consider a finite element discretization of Ω into subdomains $\Omega^e, e = 1, 2, \ldots, n_{\text{el}}$, where n_{el} is the number of elements. Based on this discretization, we define the finite element trial function space $\mathscr{S}^h$ and weighting function space $\mathscr{V}^h$. These function spaces are selected, by taking the Dirichlet boundary conditions into account, as subsets of $[\mathbf{H}^{1h}(\Omega)]^{n_{\text{dof}}}$, where $\mathbf{H}^{1h}(\Omega)$ is the finite-dimensional function space over Ω and n_{dof} is the number of degrees of freedom.

$$\begin{aligned} \mathscr{S}^h = \{ & \mathbf{U}^h | \mathbf{U}^h \in \left[\mathbf{H}^{1h}(\Omega)\right]^{n_{\text{dof}}}, \\ & \mathbf{U}^h|_{\Omega^e} \in \left[P^1(\Omega^e)\right]^{n_{\text{dof}}}, \\ & \mathbf{U}^h \cdot \mathbf{e}_k \doteq g_k \text{ on } \Gamma_{g_k} \} \ , \end{aligned} \tag{20}$$

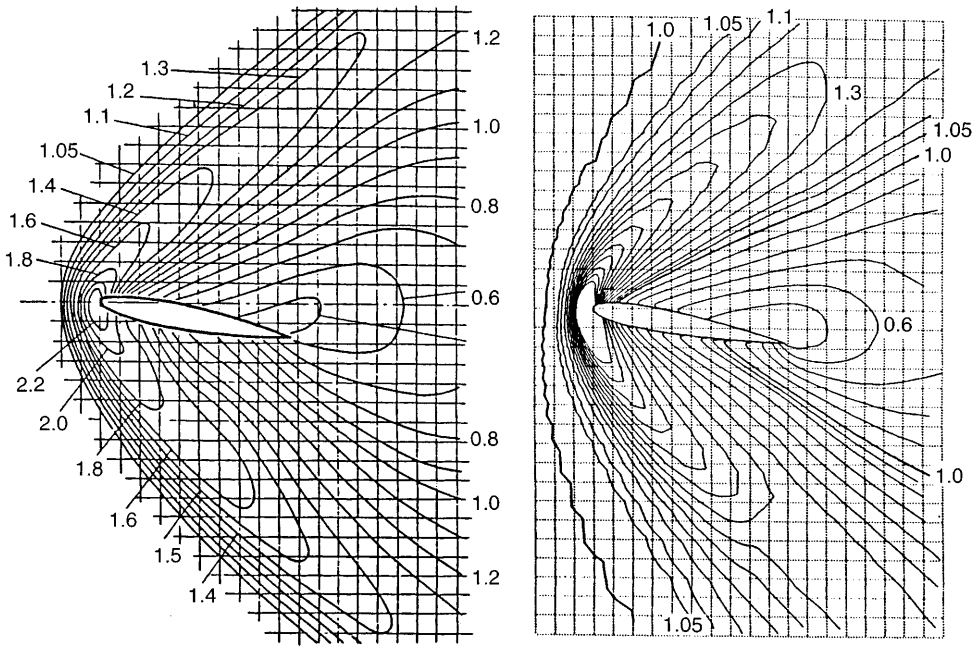

Fig. 2. $M = 2.0$, Re $= 106$, $\alpha = 10^\circ$ flow past a *NACA*0012 airfoil: density field for the steady-state solution; measurements (*left*) from Allegre et al. and numerical results (*right*) from Haase (1987)

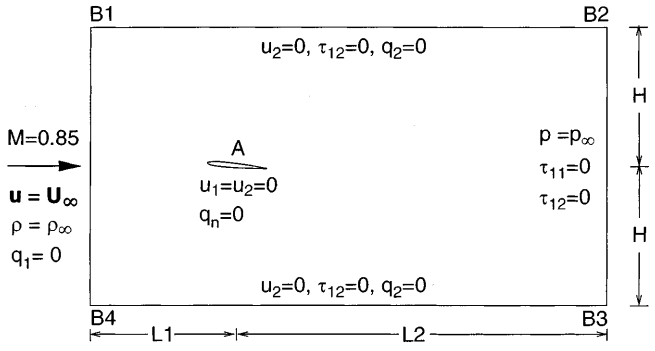

Fig. 3. Flow past an airfoil in a channel problem description

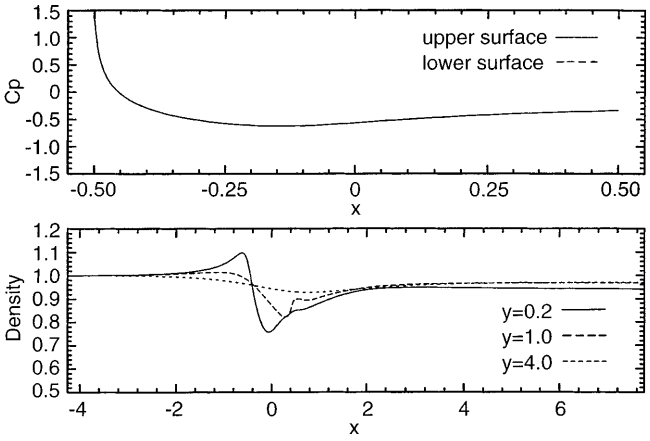

Fig. 6. Mach = 0.85, Re = 2000, $\alpha = 0^\circ$ flow past a *NACA*0012 airfoil: C_p distribution on the airfoil surface and the stream-wise variation of density in the domain at three vertical locations for the steady-state solution

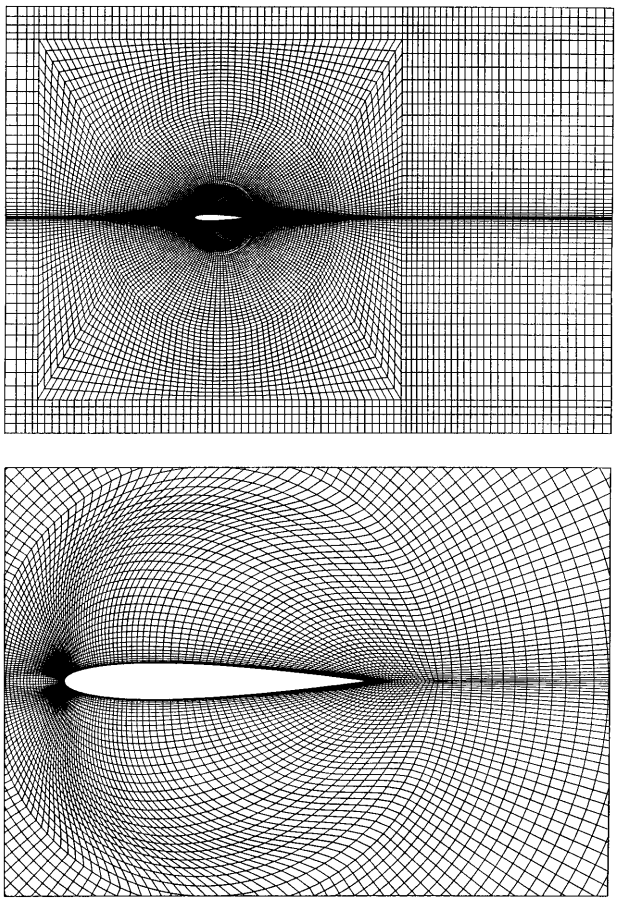

Fig. 4. Mach = 0.85, $\alpha = 0^\circ$, $H = 4.25$ flow past a *NACA*0012 airfoil: the finite element mesh; 19,014 nodes and 18,772 elements

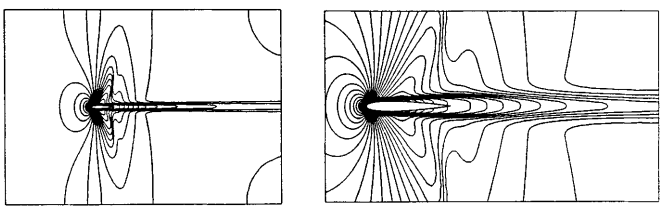

Fig. 5. Mach = 0.85, Re = 2000, $\alpha = 0^\circ$ flow past a *NACA*0012 airfoil: density field for the steady-state solution

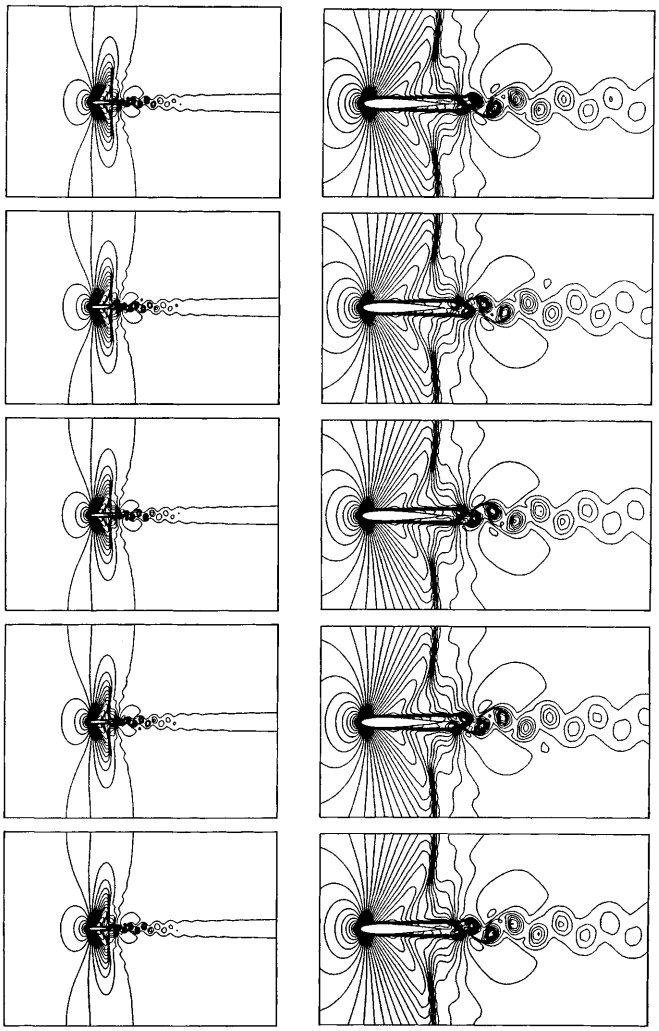

Fig. 7. Mach = 0.85, Re = 10,000, $\alpha = 0^\circ$, $H = 4.25$ flow past a *NACA*0012 airfoil: density field at five instants during one cycle of lift coefficient for the temporally periodic solution

$$\mathscr{V}^h = \left\{ \mathbf{W}^h | \mathbf{W}^h \in \left[\mathbf{H}^{1h}(\Omega)\right]^{n_{\text{dof}}}, \right.$$
$$\mathbf{W}^h|_{\Omega^e} \in \left[P^1(\Omega^e)\right]^{n_{\text{dof}}},$$
$$\left. \mathbf{W}^h \cdot \mathbf{e}_k \doteq 0 \text{ on } \Gamma_{g_k} \right\} \ , \tag{21}$$

where $[P^1(\Omega)^e)]$ represents the first order polynomial in Ω^e, and $k = 1, \ldots, n_{\text{dof}}$. The stabilized finite element formulation of Eq. (14) is written as follows: find $\mathbf{U}^h \in \mathscr{S}^h$ such that $\forall \mathbf{W}^h \in \mathscr{V}^h$,

$$\int_\Omega \mathbf{W}^h \cdot \left(\frac{\partial \mathbf{U}^h}{\partial t} + \mathbf{A}_i^h \frac{\partial \mathbf{U}^h}{\partial x_i} \right) \mathrm{d}\Omega$$
$$+ \int_\Omega \left(\frac{\partial \mathbf{W}^h}{\partial x_i} \right) \cdot \left(\mathbf{K}_{ij}^h \frac{\partial \mathbf{U}^h}{\partial x_j} \right) \mathrm{d}\Omega$$
$$+ \sum_{e=1}^{n_{\text{el}}} \int_{\Omega^e} \boldsymbol{\tau} \left(\mathbf{A}_k^h\right)^T \left(\frac{\partial \mathbf{W}^h}{\partial x_k} \right)$$
$$\cdot \left[\frac{\partial \mathbf{U}^h}{\partial t} + \mathbf{A}_i^h \frac{\partial \mathbf{U}^h}{\partial x_i} - \frac{\partial}{\partial x_i} \left(\mathbf{K}_{ij}^h \frac{\partial \mathbf{U}^h}{\partial x_j} \right) \right] \mathrm{d}\Omega$$
$$+ \sum_{e=1}^{n_{\text{el}}} \int_{\Omega^e} \delta \left(\frac{\partial \mathbf{W}^h}{\partial x_i} \right) \cdot \left(\frac{\partial \mathbf{U}^h}{\partial x_i} \right) \mathrm{d}\Omega$$
$$= \int_{\Gamma_h} \mathbf{W}^h \cdot \mathbf{h}^h \, \mathrm{d}\Gamma \ . \tag{22}$$

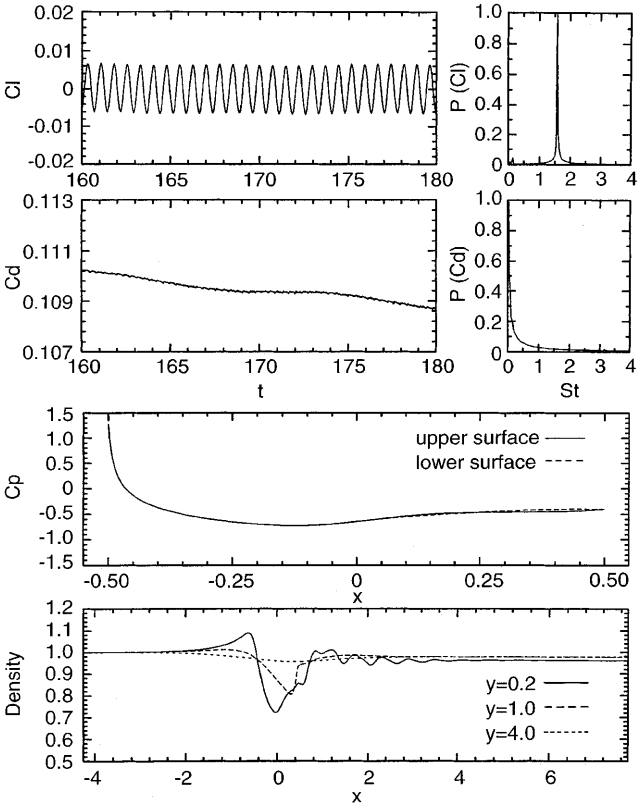

Fig. 8. Mach = 0.85, Re = 10,000, $\alpha = 0°$, $H = 4.25$ flow past a *NACA*0012 airfoil: time histories of the lift and drag coefficients, their power spectra, the C_p distribution on the airfoil surface and the stream-wise variation of the density at various vertical locations corresponding to the peak value of the lift coefficient

Remarks

1. In the variational formulation given by Eq. (22), the first two terms and the right-hand-side constitute the Galerkin formulation of the problem.

2. The first series of element-level integrals in Eq. (22) are the SUPG stabilization terms added to the variational formulation to stabilize the computations against node-to-node oscillations in the advection-dominated range. The second series of element level integrals in the formulation are the shock capturing terms that stabilize the computations in the presence of sharp gradients. The stabilization coefficients δ and $\boldsymbol{\tau}$ are quite similar to the ones that are used by Le Beau (1990) and Le Beau and Tezduyar (1991) and are defined as

$$\boldsymbol{\tau} = \max[\mathbf{0}, \boldsymbol{\tau}_a - \boldsymbol{\tau}_\delta] \ , \tag{23}$$

$$\boldsymbol{\tau}_a = \left(\left(\frac{2(c + \|\mathbf{u}\|)}{h} \right)^2 + \left(\frac{12\nu}{h^2} \right)^2 \right)^{-\frac{1}{2}} \mathbf{I} \ . \tag{24}$$

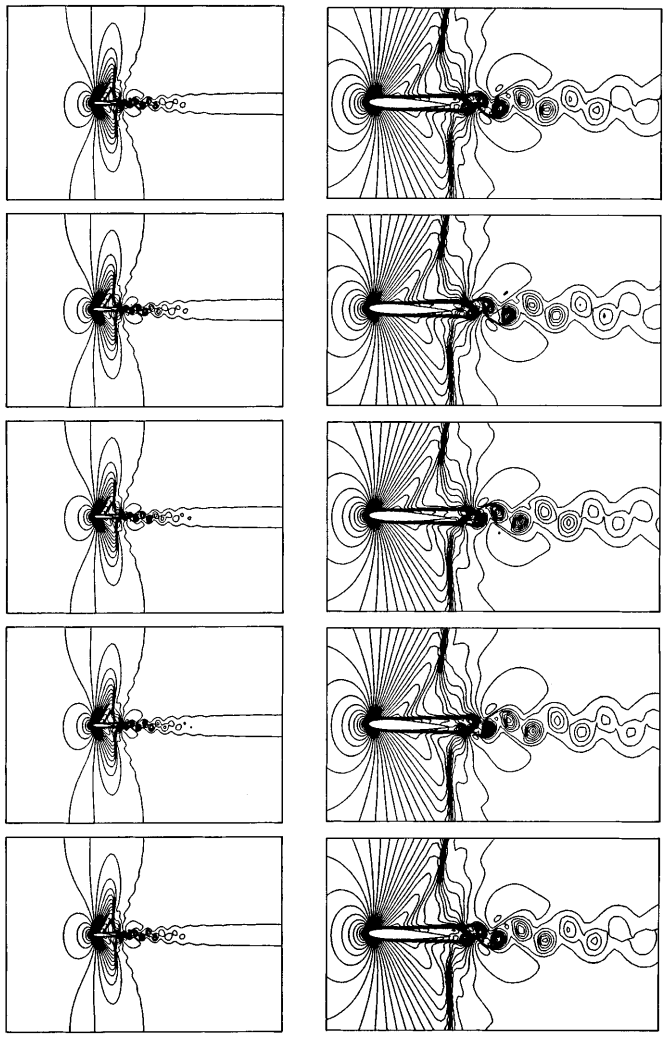

Fig. 9. Mach = 0.85, Re = 10,000, $\alpha = 2°$, $H = 4.25$ flow past a *NACA*0012 airfoil: density field at five instants during one cycle of lift coefficient for the temporally periodic solution

$$\boldsymbol{\tau}_\delta = \frac{\delta}{2(c + \|\mathbf{u}\|)^2}\mathbf{I} \ , \tag{25}$$

$$\delta = \left[\frac{\left\| \frac{\partial \mathbf{U}}{\partial t} + \mathbf{A}_i \frac{\partial \mathbf{U}}{\partial x_i} \right\|_{\mathbf{A}_0^{-1}}}{\left\| \mathbf{J}_{1i} \frac{\partial \mathbf{U}}{\partial x_i} \right\|_{\mathbf{A}_0^{-1}} + \left\| \mathbf{J}_{2i} \frac{\partial \mathbf{U}}{\partial x_i} \right\|_{\mathbf{A}_0^{-1}}} \right]^{\frac{1}{2}} , \tag{26}$$

where c is the wave speed, h is the element length, $\mathbf{J}_{jk}$ are the components of Jacobian transformation matrix from physical to the local coordinates and $\mathbf{A}_0^{-1}$ is the inverse of Reimannian metric tensor related to the transformation between the conservation and entropy variable (Hughes and Mallet 1986). Matrix $\boldsymbol{\tau}_\delta$ is subtracted from $\boldsymbol{\tau}_a$ to account for the shock-capturing term as shown in Eq. (23). The definition of δ used in Eq. (26) is the same as in (Le Beau and Tezduyar 1991; Le Beau 1990; Aliabadi 1994; Aliabadi et al. 1993) except that it includes the unsteady term in the numerator. The inclusion of this term renders consistency to the formulation, even for unsteady computations, at-least in the case of inviscid flows.

3. The time discretization of the variational formulation given by Eq. (22) is done via the generalized trapezoidal rule. For unsteady computations, we employ a second-order accurate-in-time procedure.

4
Results and discussions

All the computations reported in this article are carried out on *Digital* work-stations at *IIT Kanpur*. The method has already been tested on various benchmark problems (Le Beau and Tezduyar 1991; Aliabadi and Tezduyar 1995; Mittal 1998; Le Beau 1990; Aliabadi et al. 1993). The non-linear equation systems resulting from the finite-element discretization of the flow equations are solved using the Generalized Minimal RESidual (*GMRES*) technique (Saad and Schultz 1986) in conjunction with diagonal and block-diagonal preconditioners. Computations at each time-step involve solution for two non-linear iterations. With 10 inner iterations of the (*GMRES*) procedure the residual of the linearized equation system at each non-linear step is reduced by, approximately, three orders of magnitude. We have observed that a further increase in the number of inner (*GMRES*) iterations, although improves the convergence of the linearized algebraic equation system, does not result in any significant changes in the flow results. Sarkis et al. (1996) have reported results for a new variant

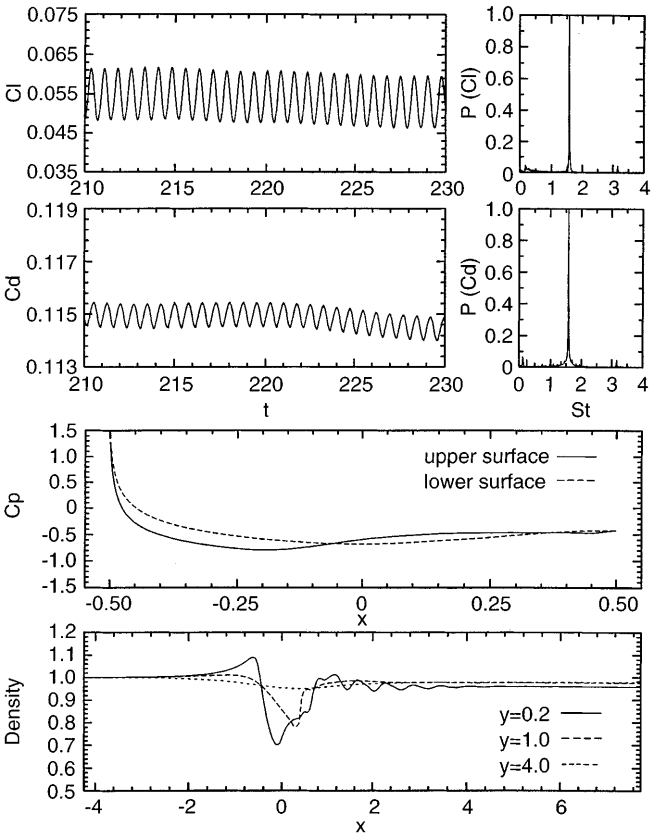

Fig. 10. Mach = 0.85, Re = 10,000, $\alpha = 2^\circ$, $H = 4.25$ flow past a *NACA*0012 airfoil: time histories of the lift and drag coefficients, their power spectra, the C_p distribution on the airfoil surface and the stream-wise variaton of the density at various vertical locations corresponding to the peak value of lift coefficient

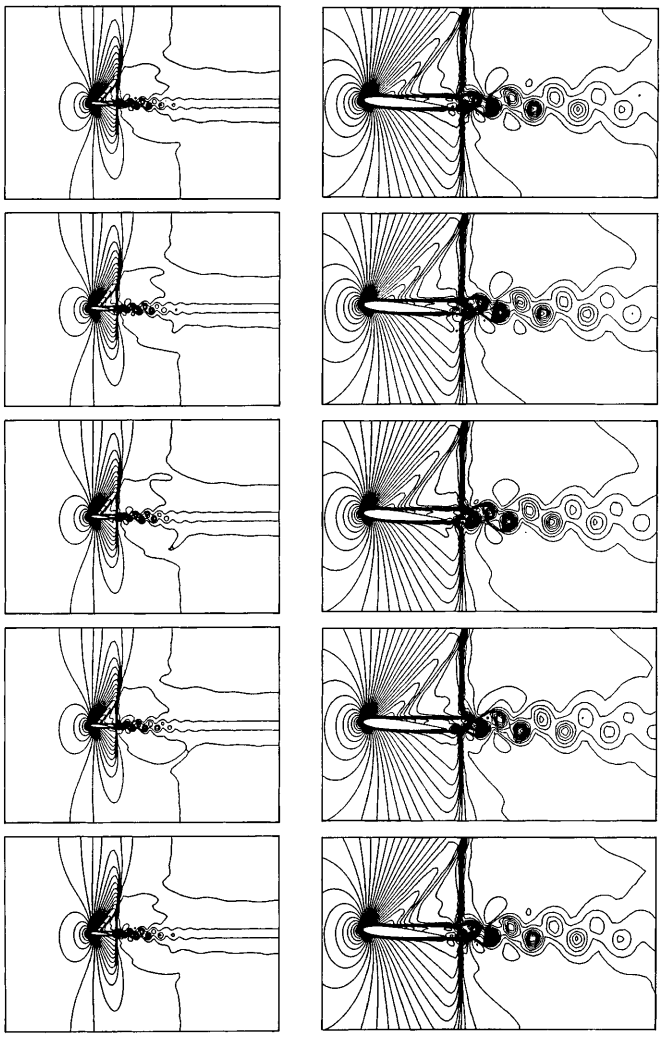

Fig. 11. Mach = 0.85, Re = 10,000, $\alpha = 5^\circ$, $H = 4.25$ flow past a *NACA*0012 airfoil: density field at five instants during one cycle of lift coefficient for the temporally periodic solution

of the Schwarz preconditioned (*GMRES*) methods for unsteady compressible flow calculations with various preconditioners and for various values of the Courant Number. The interested reader is referred to their article for an interesting discussion on the performance of various preconditioners in the context of unsteady compressible flows. For all the cases the viscosity and thermal conductivity coefficients are constant, the Prandtl Number is 0.72 and the ratio and the ratio of specific heats, γ, is 1.4. The Reynolds number is based on the chord of the airfoil, the free-stream velocity and kinematic viscosity.

4.1
Mach = 2, Re = 106, $\alpha = 10^\circ$ flow past a *NACA0012* airfoil

Experimental results for this flow are available (Bristeau et al. 1988; Allegre et al. 1987) and, therefore, this case has become a standard test problem. The airfoil surface is assumed to be adiabatic and the no-slip condition is specified for the velocity on its wall. All the variables are specified on the upstream boundary. At the downstream boundary the viscous stress and heat flux vectors are assigned a zero value. On the lateral boundaries the components of velocity and heat flux normal to and the component of viscous stress vector along these boundaries are prescribed zero values. The upstream and downstream boundaries are located at 4.25 and 7.75 chord-lengths, respectively, from the mid-chord point of the airfoil. The lateral boundaries are located at 12 chord-lengths, each from the airfoil. The computations are initiated with free-stream conditions in the entire domain. Figure 1 shows the density field for the steady state solution. Shown in Fig. 2 are the density fields from laboratory experiments and numerical results from other researchers (Bristeau et al. 1988; Allegre et al. 1987; Haase 1987). It can be observed that the present solutions compare quite well with those obtained by others. The steady state drag and lift coefficients for the present solution are 0.496 and 0.333, respectively. The value of drag coefficient reported by other researchers varies between 0.41–0.49 while that for lift coefficient is between 0.31–0.41 (Haase 1987; Bristeau et al. 1987; Bassi et al. 1988).

4.2
Mach = 0.85 flow past a *NACA*0012 airfoil

A *NACA0012* airfoil is placed in a Mach 0.85 flow. Figure 3 shows the boundary conditions that are prescribed for the simulations. The airfoil surface (A) is assumed to be

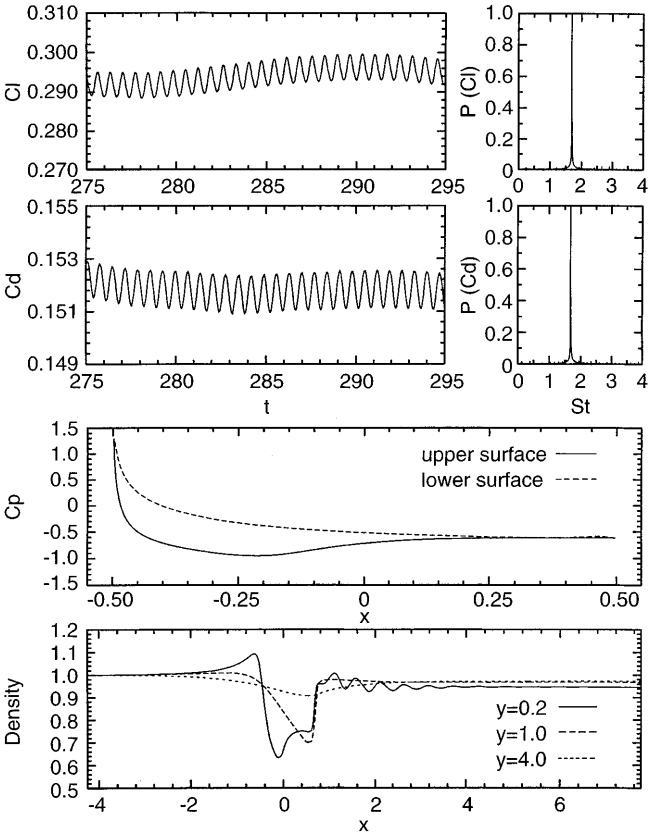

Fig. 12. Mach = 0.85, Re = 10,000, $\alpha = 5^\circ$, $H = 4.25$ flow past a *NACA*0012 airfoil: time histories of the lift and drag coefficients, their power spectra, the C_p distribution on the airfoil surface and the stream-wise variation of the density at various vertical locations corresponding to the peak value of the lift coefficient

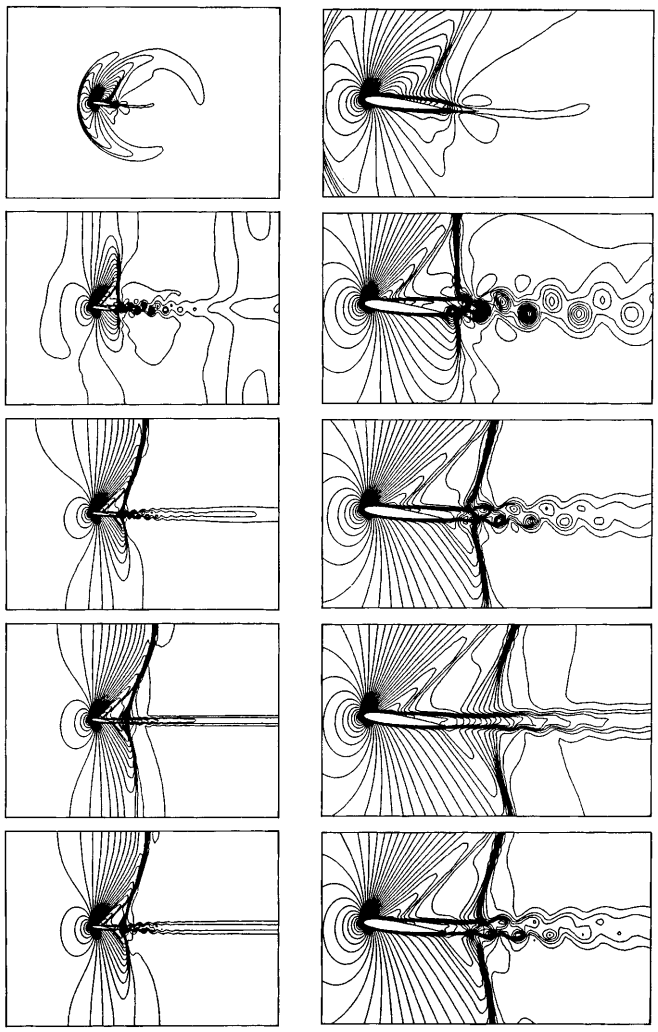

Fig. 13. Mach = 0.85, Re = 10,000, $\alpha = 7^\circ$, $H = 4.25$ flow past a *NACA*0012 airfoil: density field at $t = 2.3$, 43.1, 104.7, 226.4, 654.6

adiabatic and the no-slip condition is specified for the velocity on its wall. At the upstream boundary ($B1$–$B4$), density and both components of velocity are assigned free-stream values while the component of heat flux vector normal to the boundary is assumed to be zero. At the downstream boundary ($B2$–$B3$), the pressure is prescribed while the viscous stress vector is assigned zero value. On the upper and lower boundaries ($B1$–$B2$ and $B3$–$B4$), the components of velocity and heat flux vector normal to and the component of viscous stress vector along these boundaries are prescribed zero values. The airfoil is located at the origin of the coordinate axes. The location of the upstream and downstream boundaries, from the mid-chord point of the airfoil, correspond to $L1 = 4.25$ and $L2 = 7.75$ chord-lengths, respectively. Unless specified, the computations are initiated with free-stream conditions in the entire domain. A time step of 0.01 is used to ensure time accuracy of the results. The chord-length of the airfoil, the free-stream speed, temperature and density of the flow are used to non-dimensionalize the various quantities. On a *Digital* 250-4/266 work-station, each time-step takes approximately 1 minute of *CPU* time.

Computations are carried out for two locations of the lateral boundaries. In the first case the upper and lower boundaries are, each, located at $H = 4.25$ chord-lengths away from the mid-chord point of the airfoil. The mesh employed consists of 18,772 quadrilateral elements and 19,014 nodes. It is observed that when the angle of attack of the airfoil, with respect to the free-stream flow, is 5° and above there is significant interaction between the flow and the lateral boundaries. In the second case, the lateral boundaries are, each, located at $H = 12$ chord-lengths away from the mid-chord point of the airfoil. The finite-element mesh, for this case, consists of 22,132 elements and 22,414 nodes. For both the cases, the mesh close to the airfoil, is same. The mesh for the first case, and its close-up, is shown in Fig. 4.

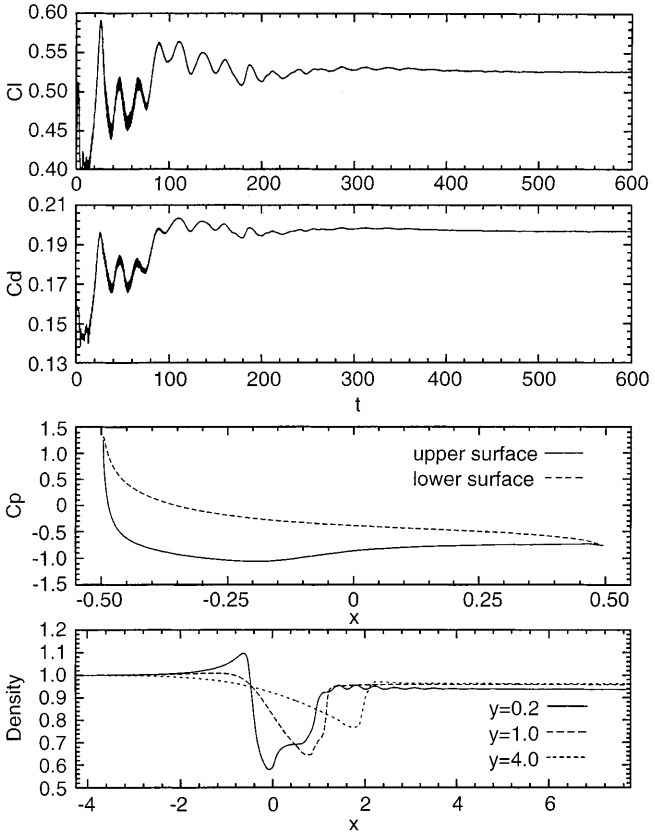

Fig. 14. Mach = 0.85, Re = 10,000, $\alpha = 7°$, $H = 4.25$ flow past a *NACA*0012 airfoil: time histories of the lift and drag coefficients, the C_p distribution on the airfoil surface and the stream-wise variation of the density at various vertical locations corresponding to the temporally periodic solution at $t = 654.6$

4.2.1
Mach = 0.85, Re = 2000, $\alpha = 0°$ flow past a *NACA*0012 airfoil

This is a standard benchmark problem from one of the *GAMM* workshops (Bristeau et al. 1988). At this Reynolds number the present computations converge to a steady-state solution. Shown in Fig. 5 is the density field for the steady-state solution. These solutions agree quite well with the ones reported by other researchers (Bristeau et al. 1988; Boivin and Fortin 1993). The steady-state drag coefficient is 0.15. The value of drag coefficient reported by other researchers varies between 0.1–0.14 (Bristeau et al. 1987). Figure 6 shows the pressure distribution on the airfoil surface and the stream-wise variation of density in the domain at three vertical locations. It is observed that the flow is symmetric about the chord-line of the airfoil. Unlike the case of Euler solution, in the present case, the presence of shock does not lead to a jump in the pressure on the airfoil surface. More details on this calculation and comparison of results for various other cases, with experimental and numerical results from other researchers, are given in Mittal (1998).

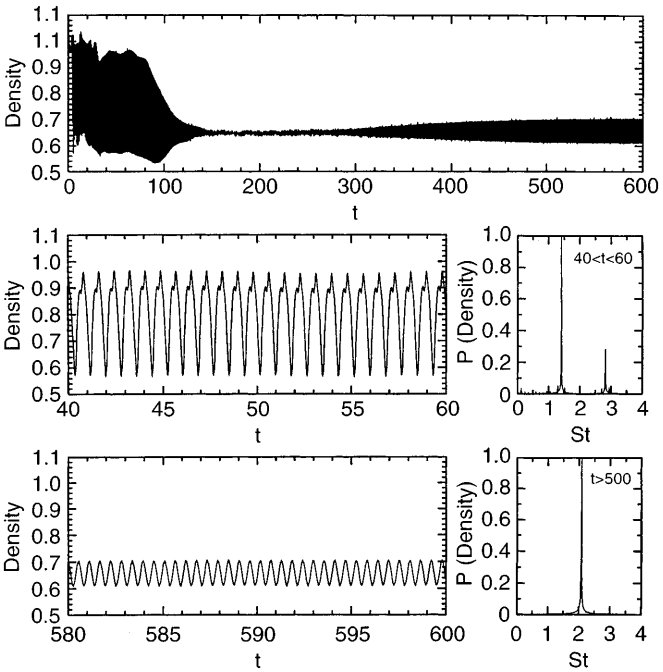

Fig. 15. Mach = 0.85, Re = 10,000, $\alpha = 7°$, $H = 4.25$ flow past a *NACA*0012 airfoil: time history of the density, and its power spectrum, recorded by a probe located at (0.462, −0.044) with respect to the center of the airfoil

4.2.2
Mach = 0.85, Re = 10,000, flow past a *NACA*0012 airfoil; $H = 4.25$

This case corresponds to transonic flow past an airfoil in a channel or a wind-tunnel. Solutions are computed for various values of the angle of attack of the airfoil. It is observed that at low angles of attack ($\alpha = 0^\circ, 2^\circ$) the lateral boundaries do not interact with the flow significantly. At $\alpha = 5^\circ$ and beyond the effect of the side-walls becomes important and leads to interesting solutions. At $\alpha = 8^\circ$ 'hysteresis' is observed, i.e., one obtains two different stable solutions depending on the initial conditions of the simulation.

Figure 7 shows the density field at five instants during one cycle of lift coefficient for the temporally periodic solution at $\alpha = 0^\circ$. The interaction between the shock and expansion waves, and the boundary and shear layers can be clearly observed. Downstream of the nose of the airfoil, the flow expands till, approximately, the mid-chord point. By this point, the boundary layer thickness increases causing the flow to constrict, resulting in the formation of a weak oblique shock. The interaction between the boundary layer and shock wave results in the separation of flow and one can observe the formation of a shear layer downstream of the shock. Another shock is formed further downstream that combines with the shock and expansion waves formed upstream resulting in a lambda shock. One vortex shed alternately from each of the upper and lower surfaces of the airfoil constitutes one cycle of vortex-shedding. These flow patterns compare quite well with the computational results reported in Bristeau et al. 1988 and with the experimental results reported in Shapiro (1958, p. 414). It must be pointed out that the laboratory experiments (Shapiro 1958) correspond to a much larger Reynolds number. Figure 8 shows the time histories of the lift and drag coefficients, their power spectra, the C_p distribution on the airfoil surface and the stream-wise variation of the density at various vertical locations

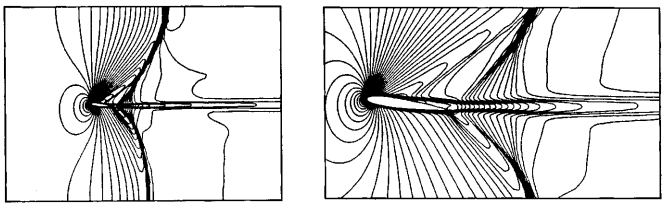

Fig. 16. Mach = 0.85, Re = 10,000, $\alpha = 8^\circ$, $H = 4.25$ flow past a *NACA*0012 airfoil: density field for the steady-state solution

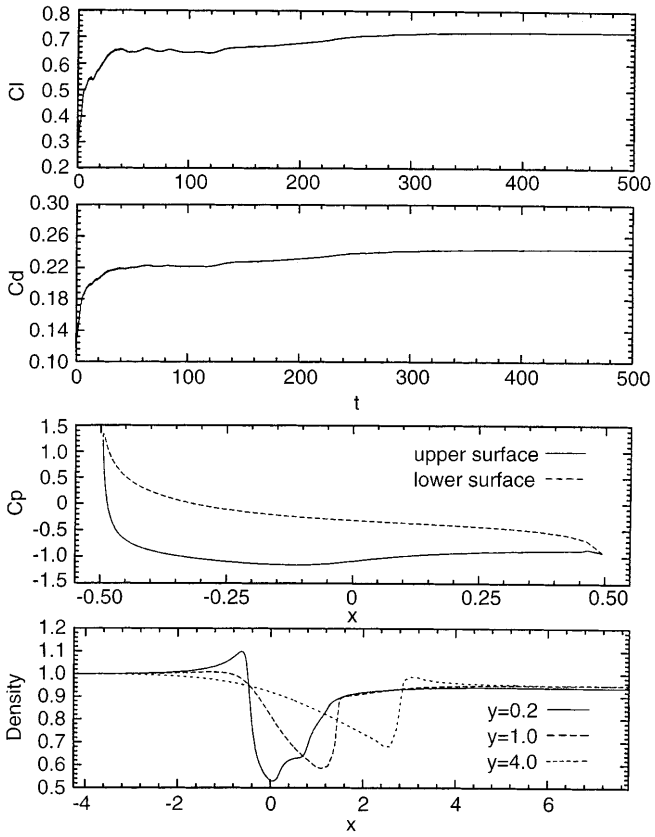

Fig. 17. Mach = 0.85, Re = 10,000, $\alpha = 8^\circ$, $H = 4.25$ flow past a *NACA*0012 airfoil: time histories of the lift and drag coefficients, C_p distribution on the airfoil surface and the stream-wise variation of density in the domain at three vertical locations for the steady-state solution

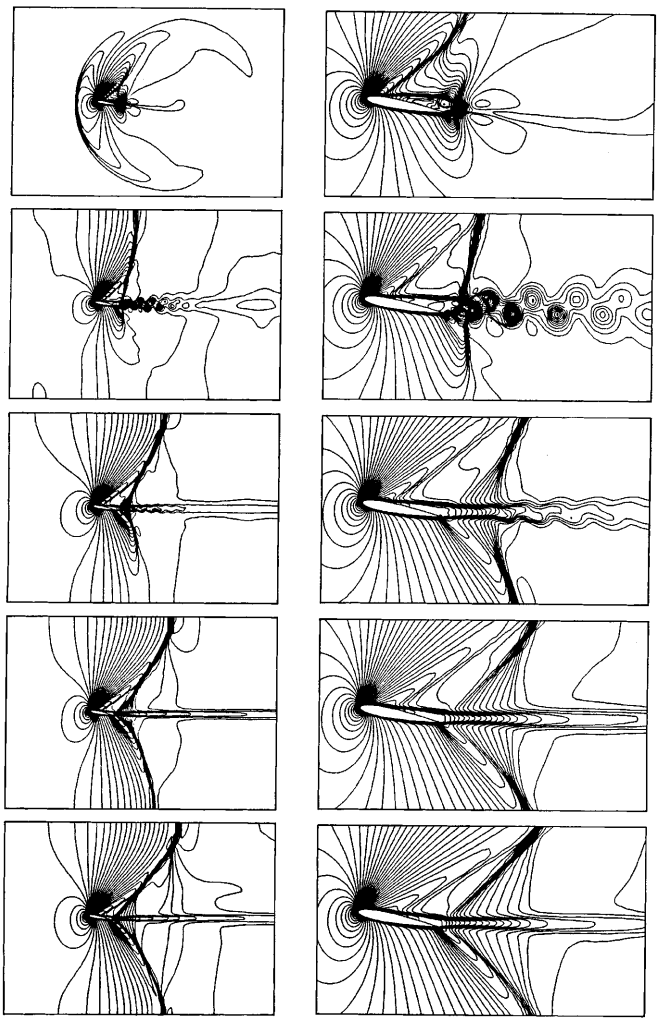

Fig. 18. Mach = 0.85, Re = 10,000, $\alpha = 10^\circ$, $H = 4.25$ flow past a *NACA*0012 airfoil: density field at $t = 3.6, 50.3, 100.3, 120.3, 150.3$

corresponding to the peak value of the lift coefficient. The Strouhal number corresponding to the lift coefficient variation is 1.58 while the drag coefficient is almost constant during each cycle of vortex shedding. In Fig. 7, from the pictures showing the flow close to the airfoil, it can be observed that the unsteadiness in the pressure felt by the airfoil surface, due to vortex shedding, is confined to a small region near the trailing edge. For $\alpha = 0$, the airfoil surface close to the trailing edge is almost in the free-stream direction and therefore, the unsteady pressure forces contribute mainly to the unsteadiness in lift and have a negligible effect on the time-variation of the drag force. It should be noted that the chord-length of the airfoil (and not its thickness) has been used to obtain the non-dimensional quantities. If the Strouhal number is non-dimensionalized with respect to the thickness of the airfoil than one obtains a value of 0.19. Notice that this value of the Strouhal number is very close to the one for a bluff-body in an incompressible flow. This observation is consistent with that made by other researchers that it is possible to define a 'universal' Strouhal number for any section based on the separation distance between shear layers. The effect of vortex shedding and the shocks/expansion waves can be clearly observed in the plot of stream-wise density variation. The effect is mostly felt close to the airfoil surface while far away, close to the upper wall, the effect is negligible.

Solutions for flow at angle of attack 2° is shown in Figs. 9 and 10. The asymmetry between the flows on the upper and lower surfaces of the airfoil is clearly visible. Compared to the flow for $\alpha = 0°$ the unsteadiness in the flow is stronger. Also, the lambda shock on the upper surface is stronger compared to the previous case. This can also be observed from the comparison of the stream-wise density distribution for the two cases. The effect of the presence of the airfoil on the density at $y = 4$, close to the upper wall, is still quite negligible. The Strouhal number corresponding to the lift coefficient variation has the same value as for $\alpha = 0°$ case. The drag coefficient also oscillates with the same frequency as the lift coefficient. This is in quite contrast to the observation one makes for flows past bluff bodies where the drag coefficient oscillates at twice the frequency of the lift coefficient. Recall, the unsteady flow past a circular cylinder involves flow separation at both, the lower and upper surfaces. During each cycle of the temporal variation of the lift coefficient the unsteadiness on both the lower and upper surfaces contribute to the

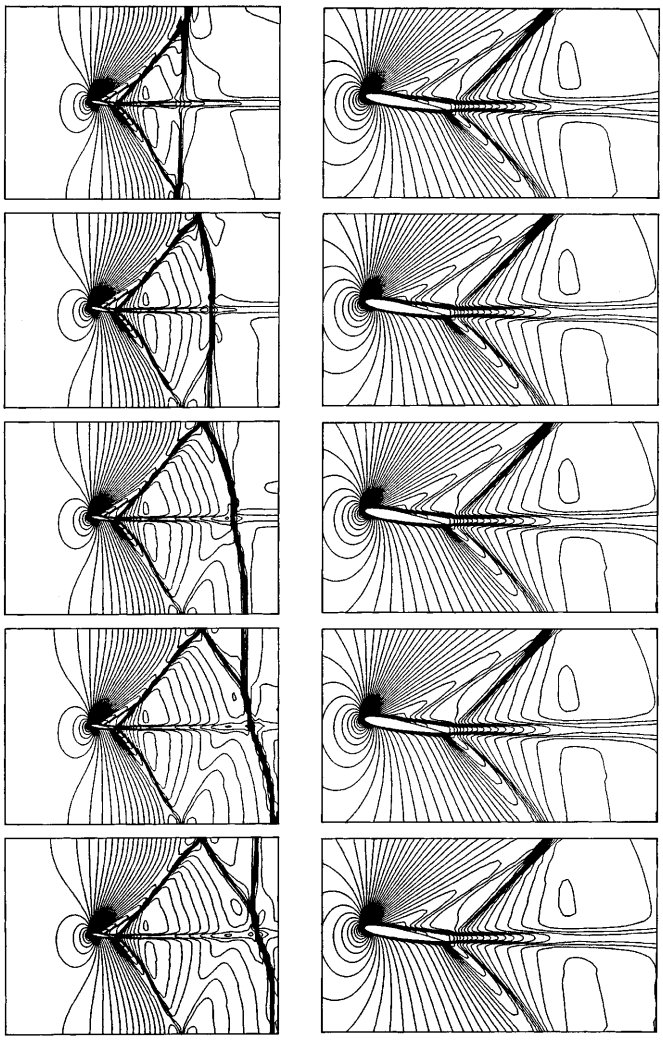

Fig. 19. Mach = 0.85, Re = 10,000, $\alpha = 10°$, $H = 4.25$ flow past a *NACA*0012 airfoil: density field at $t = 200.3$, 300.3, 400.3, 500.3, 645.5

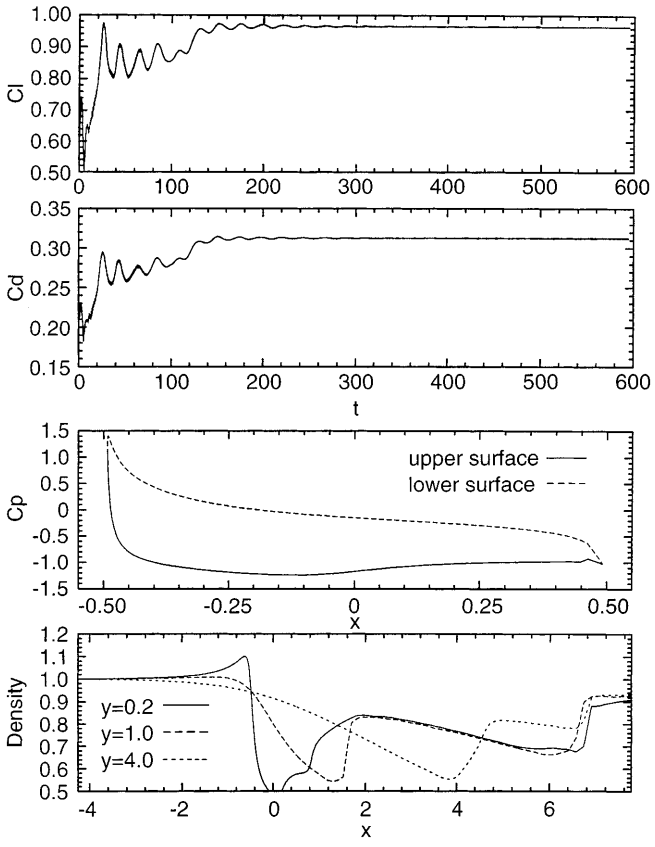

Fig. 20. *Mach* = 0.85, *Re* = 10,000, $\alpha = 10°$, $H = 4.25$ flow past a *NACA*0012 airfoil: time histories of the lift and drag coefficients, C_p distribution on the airfoil surface and the stream-wise variation of density in the domain at three vertical locations for the steady-state solution

unsteadiness in the drag coefficient. On the other hand, for flow past an airfoil at an angle of attack, one observes separation of flow only on the upper surface while the flow on the lower surface is attached and steady. Therefore, the drag coefficient oscillates at the same frequency as the lift coefficient.

Figures 11 and 12 show the solution for flow at $\alpha = 5°$. Compared to the previous cases, lambda shock becomes even stronger. This can be seen from both, the iso-density contours in Fig. 11 and from stream-wise variation in density at various vertical locations in Fig. 12. Additionally, in this case, the effect of shock on the upper wall is not negligible as can be observed from the plot of stream-wise variation of density at $y = 4$. The Strouhal number corresponding to the lift and drag coefficient variation is 1.69. This value is higher than that in the previous cases. It will be seen later that when the distance between the airfoil and the lateral boundaries is increased the Strouhal number for the resulting flow has a much lower value. Therefore, it can be concluded that the interaction between the shock and the upper wall is responsible for the increased Strouhal number.

At $\alpha = 7°$ the interaction between the lateral boundaries and the shocks increases even further and leads to very interesting observations. Figure 13 shows the density field for the solution at various time instants during the simulation. At $t = 2.3$ one can see the upstream propagation of the initial bow-shock. A lambda shock forms on the upper surface of the airfoil. At $t = 43.1$ the lambda shock is quite well developed and one can observe the von Karman vortex street in the wake of the airfoil. The lambda shock develops even further by $t = 104.7$ and extends up to the upper wall. Beyond $t = 100$ the flow quantities on the surface of the airfoil do not change much while the wake and rear part of the lambda shock go through some changes. At $t = 226.4$ the downstream part of the lambda shock becomes weaker. This causes a decrease in the adverse pressure gradient as a result of which the unsteadiness in the wake decreases. Beyond $t = 300$, the flow in the near wake, close to the airfoil, does not go through any significant change. At approximately $t = 500$ the flow reaches a temporally periodic state. The last two frames of Fig. 13 show the density field corresponding to the temporally periodic solution at $t = 654.6$. Figure 14 shows the time histories of the lift and drag coefficients the C_p

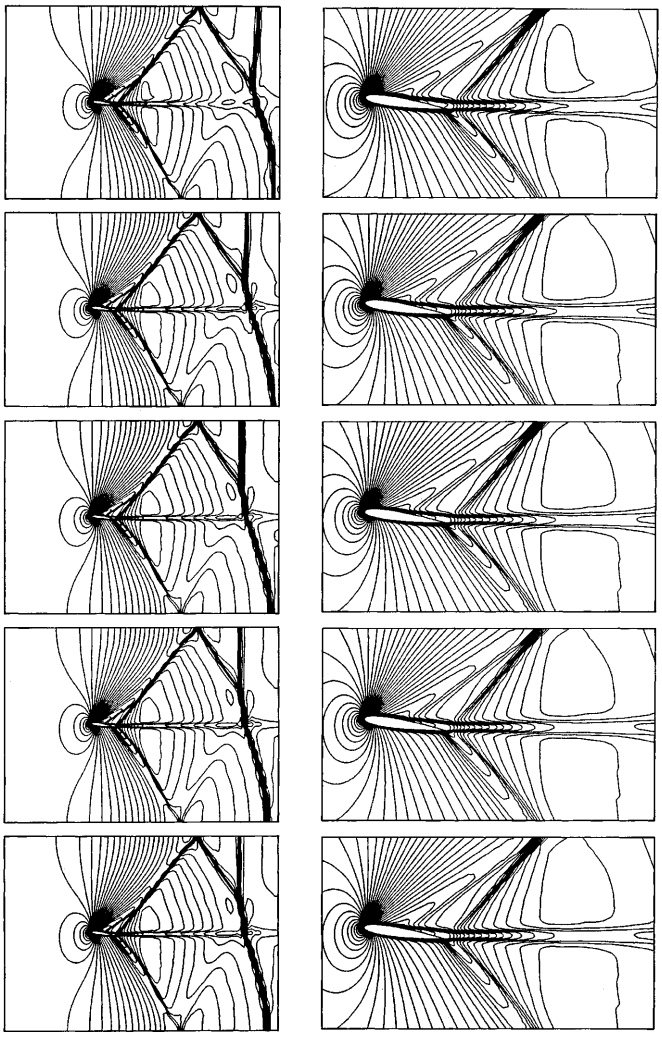

Fig. 21. Mach = 0.85, Re = 10,000, $\alpha = 8°$, $H = 4.25$ flow past a *NACA*0012 airfoil: density field at $t = 29.4$, 97.1, 187.1, 263.7, 327.4. The steady-state solution at $\alpha = 10°$ (see Fig. 19) is used as an initial condition

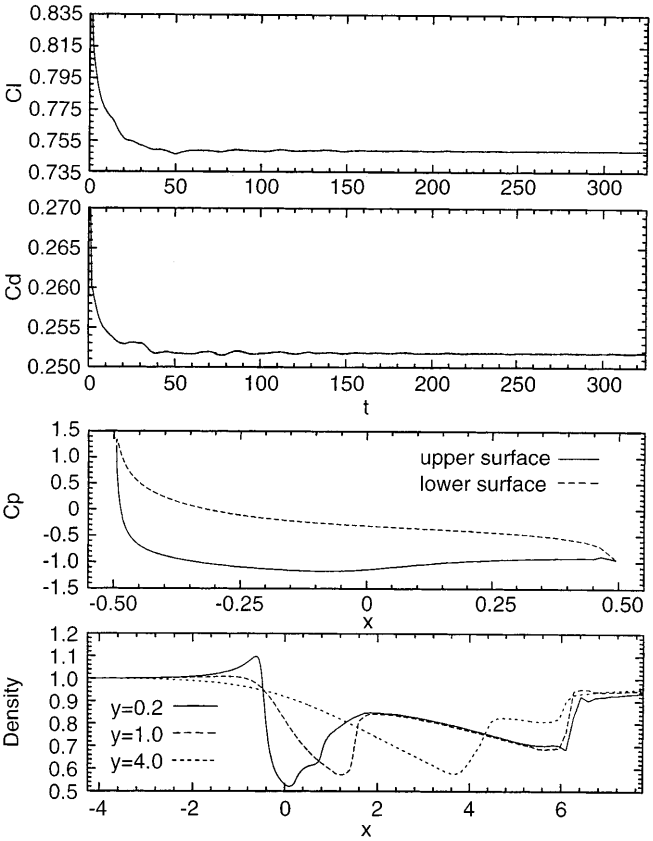

Fig. 22. Mach = 0.85, Re = 10,000, $\alpha = 8°$, $H = 4.25$ flow past a *NACA*0012 airfoil: time histories of the lift and drag coefficients, C_p distribution on the airfoil surface and the stream-wise variation of density in the domain at three vertical locations for the steady-state solution. The steady-state solution at $\alpha = 10°$ (see Fig. 19) is used as an initial condition

distribution on the airfoil surface and the stream-wise variation of the density at various vertical locations for the temporally periodic solution. The lift and drag coefficients reach a steady-state value at approximately $t = 300$. This observation is consistent to the one that was made with regards to the flow field. From the plot for the stream-wise variation of density at various locations it can be observed that the lambda shock is significantly stronger in this than at lower angles of attack. However, the unsteadiness in the wake is much lower at $\alpha = 7^\circ$. Additionally, the shock extends all the way up to the upper wall and this can also be seen from the jump in the density for $y = 4$. Figure 15 shows the time history of the density recorded by a probe located at (0.462,–0.044) with respect to the center of the airfoil. Also shown in the figure are the power spectra of the density variation for $40 \leq t \leq 60$ and $500 \leq t \leq 600$. In the initial stages of the simulation, when the shock has still not reached the upper wall, the Strouhal number corresponding to the dominant frequency of density variation is 1.41 which is quite clsoe to the one for flows at lower angles of attack. However, for the temporally periodic solution, the Strouhal number is 2.08. The effect of these temporal variations in the wake is quite negligible on the lift and drag coefficients.

Computations at $\alpha = 8^\circ$ show a similar behavior as for $\alpha = 7^\circ$ except that the flow finally reaches a steady-state. The density field for the final steady solution is shown in Fig. 16. It can be observed that for this case the shocks extend to both the lateral boundaries. Compared to the solution at $\alpha = 7^\circ$, the expansion fan at the front half of the airfoil is much stronger for this case, while the downstream branch of the lambda shock, close to the airfoil surface, is a much more gradual compression. Therefore, the shear layer emanating from the upper surface of the airfoil remains stable and results in a steady wake. Figure 17 shows the time histories of the lift and drag coefficients, the C_p distribution on the airfoil surface and the stream-wise variation of the density at various vertical locations for the steady-state solution.

Figures 18 and 19 show the density field at various time instants during the simulation for the $\alpha = 10^\circ$ case. At $t = 3.6$ one can observe the upstream propagation of the initial bow-shock and the development of the shock and shear layers. At $t = 50.3$ the lambda shock is formed and the von Karman vortex street develops in the wake. The Strouhal number corresponding to the dominant fre-

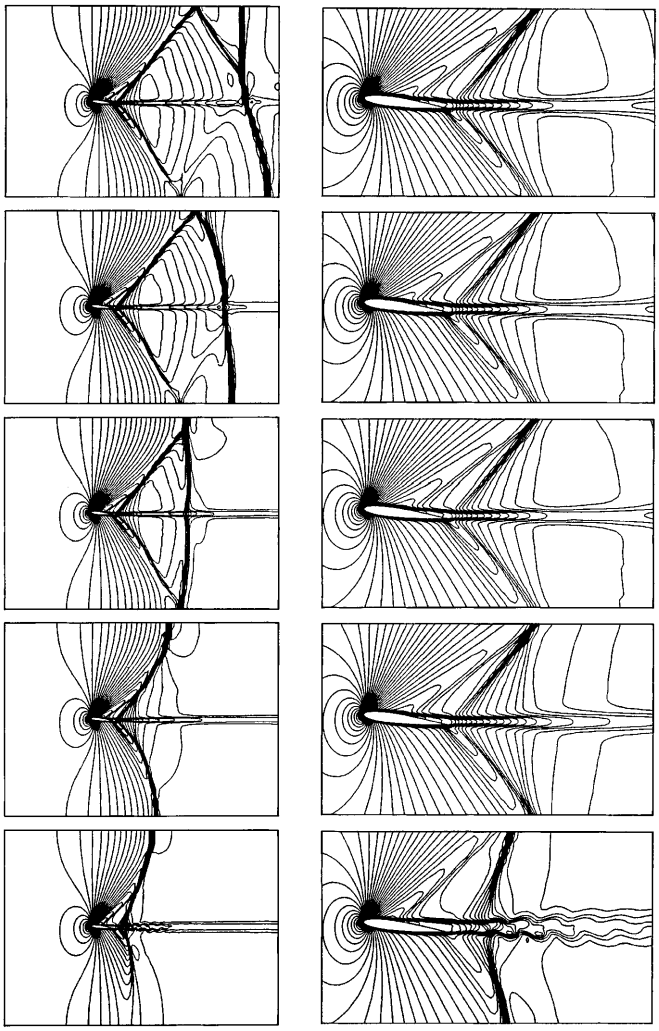

Fig. 23. Mach = 0.85, Re = 10,000, $\alpha = 7^\circ$, $H = 4.25$ flow past a *NACA*0012 airfoil: density field at $t = 20.0$, 296.4, 590.2, 798.5, 1118.5. The steady-state solution at $\alpha = 8^\circ$ (see Fig. 21) is used as an initial condition

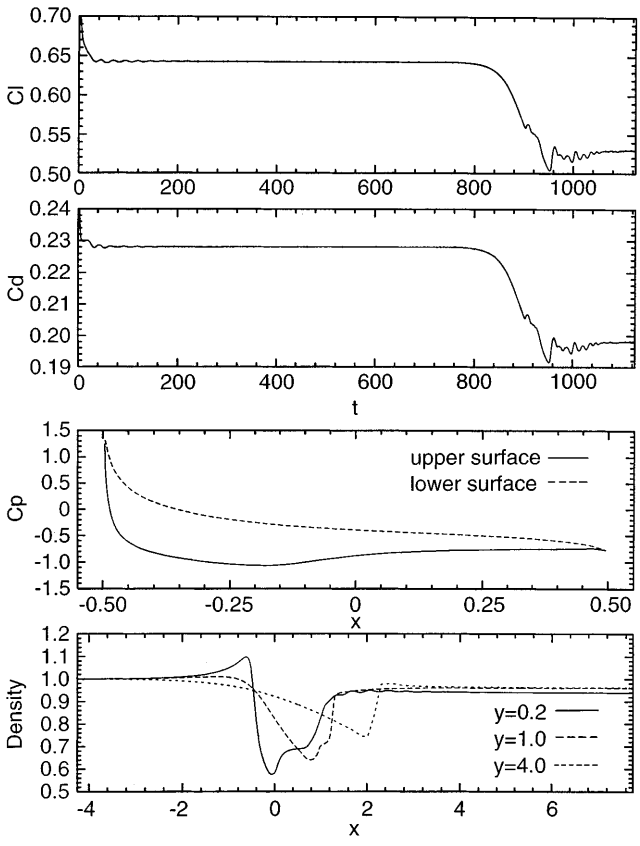

Fig. 24. *Mach* = 0.85, *Re* = 10,000, $\alpha = 7^\circ$, $H = 4.25$ flow past a *NACA*0012 airfoil: time histories of the lift and drag coefficients, C_p distribution on the airfoil surface and the stream-wise variation of density in the domain at three vertical locations for the solution at $t = 1100$. The steady-state solution at $\alpha = 8^\circ$ (see Fig. 21) is used as an initial condition

quency of lift coefficient is, approximately, 1.5. At later times, the expansion fan on the front part of the airfoil becomes stronger while the downstream branch of the lambda shock, close to the airfoil surface, transforms into a much more gradual compression. Therefore, the shear layer emanating from the upper surface of the airfoil remains stable and results in a steady wake. At $t = 120.3$ the wake becomes steady and the solution looks quite similar to the one for the $\alpha = 8^\circ$ case. However, this shock structure is unstable and at $t = 150.3$ one can observe the development of a reflection shock. Figure 19 shows the various stages of development of the reflection shock and the steady-state solution. It is interesting to notice that the near field solution, close to the airfoil, remains steady beyond $t = 150$. Figure 20 shows the time histories of the lift and drag coefficients, the C_p distribution on the airfoil surface and the stream-wise variation of the density at various vertical locations for the steady-state solution.

The next computation, for $\alpha = 8^\circ$, reveals the interesting phenomenon of hysteresis. Using the solution from the previous case for $\alpha = 10^\circ$ as an initial condition, the angle of attack of the airfoil is changed from $\alpha = 10^\circ$ to $\alpha = 8^\circ$ in 200 time steps. Recall, all the computations in the earlier cases were initiated with free-stream conditions in the entire domain. Figure 21 shows the steady-state density field and the ones at various item instants during the simulation. The final solution is quite similar to the one at $\alpha = 10^\circ$. Compared to the solution in Fig. 16, where the computations are initiated with free-stream conditions in the entire domain, two major differences are observed. Unlike the flow in Fig. 16, the present solution involves a system of shocks reflected from the lateral boundaries. The downstream branch of the lambda shock, close to the airfoil surface, results in a much more gradual compression, in the present case. However, the near field solution, very close to the airfoil, is quite similar in the two cases. Figure 22 shows the time histories of the lift and drag coefficients, the C_p distribution on the airfoil surface and the stream-wise variation of the density at various vertical locations for the steady-state solution. On comparing Fig. 17 and 22 it can be observed that the steady-state values of the lift and drag coefficients and the C_p distribution on the airfoil surface are very close for the two cases. These computations suggest that if a corresponding experiment is conducted in a wind-tunnel then it is possible to see two stable solutions for $\alpha = 8^\circ$ depending on whether one achieves the flow by keeping $\alpha = 8^\circ$ and then

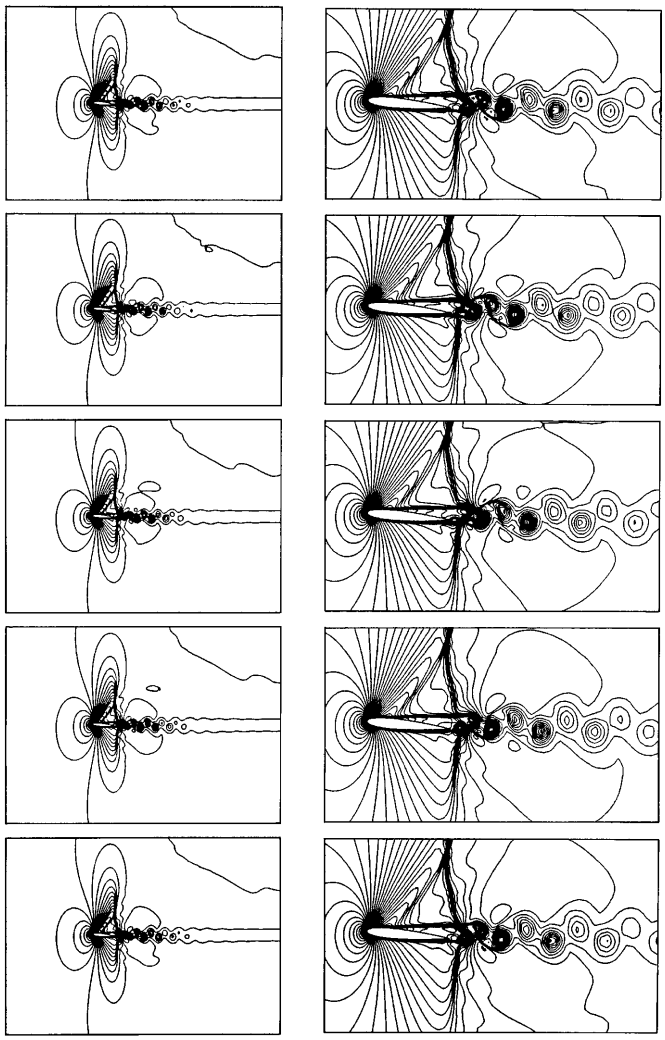

Fig. 25. *Mach* = 0.85, *Re* = 10,000, $\alpha = 5^\circ$, $H = 12$ flow past a *NACA*0012 airfoil: density field at five instants during one cycle of lift coefficient for the temporally periodic solution

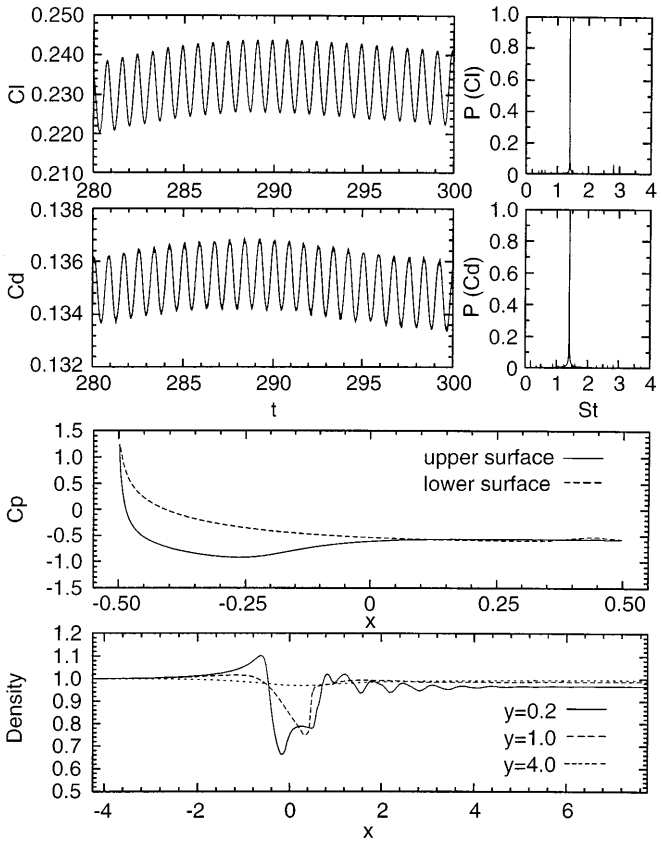

Fig. 26. *Mach* = 0.85, *Re* = 10,000, $\alpha = 5^\circ$, $H = 12$ flow past a *NACA*0012 airfoil: time histories of the lift and drag coefficients, their power spectra, the C_p distribution on the airfoil surface and the stream-wise variation of the density at various vertical locations corresponding to the peak value of the lift coefficient

starting the tunnel or by decreasing the angle of attack in an already developed flow at a larger α. However, it should be pointed out that there are differences between the initial conditions employed for the present calculations and the start-up conditions for a real wind-tunnel.

In the next simulation, the solution from the previous case for $\alpha = 8^\circ$ is used as an initial condition and in 200 time steps the angle of attack of the airfoil is changed from $\alpha = 8^\circ$ to $\alpha = 7^\circ$. Figure 23 shows the density field at various time instants during the simulation. At $\alpha = 7^\circ$ the reflection shock solution is not stable and it degenerates to the temporally periodic solution as obtained in the previous case when the computations are initiated with the free-stream conditions in the entire domain (Fig. 13). Figure 24 shows the time histories of the lift and drag coefficients, the C_p distribution on the airfoil surface and the stream-wise variation of the density at various vertical locations for the solution at $t = 1100$.

Starting from the solution at $\alpha = 7^\circ$, as the angle of attack is decreased further, the resulting solutions resemble the ones obtained earlier when the computations are initiated with the free-stream conditions in the entire domain. Therefore, for the present case, hysteresis is observed only at $\alpha = 8^\circ$. Perhaps, in reality, there is a range of values around $\alpha = 8^\circ$ where this phenomenon can be observed. Locating this band of α will form an interesting study. It is also expected that the behaviour of the flow for various angles of attack strongly depends on the location of the lateral boundaries.

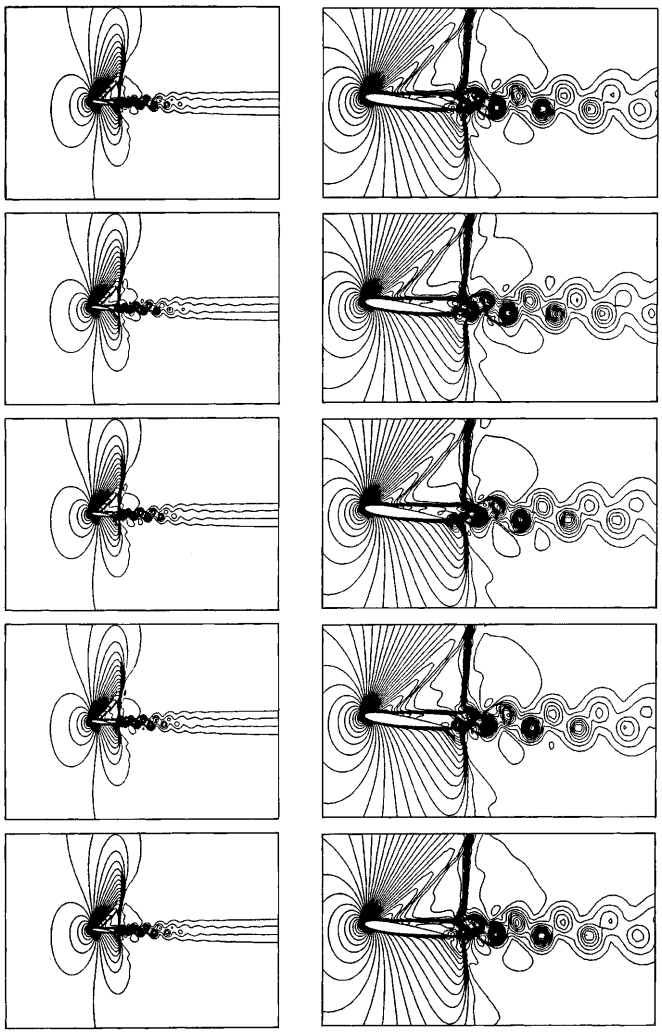

Fig. 27. Mach = 0.85, Re = 10,000, $\alpha = 8^\circ$, $H = 12$ flow past a *NACA*0012 airfoil: density field at five instants during one cycle of lift coefficient for the temporally periodic solution

4.2.3 *Mach* = 0.85, *Re* = 10,000, flow past a *NACA*0012 airfoil; *H* = 12

In the previous section it was seen that at α beyond 2° the interaction between the lateral boundaries and the flow becomes quite significant. To study the flow past an airfoil in 'free-flight' conditions the lateral boundaries are moved farther away ($H = 12$, refer to Fig. 3). Figure 25 shows the density field at five instants during one cycle of lift coefficient for the temporally periodic solution at $\alpha = 5^\circ$ computed on the extended domain. The figures show solutions on same part of the domain as before, to assist in comparison with the solutions obtained in previous section. Figure 26 shows the time histories of the lift and drag coefficients, their power spectra, the C_p distribution on the airfoil surface and the stream-wise variation of the density at various vertical locations corresponding to the peak

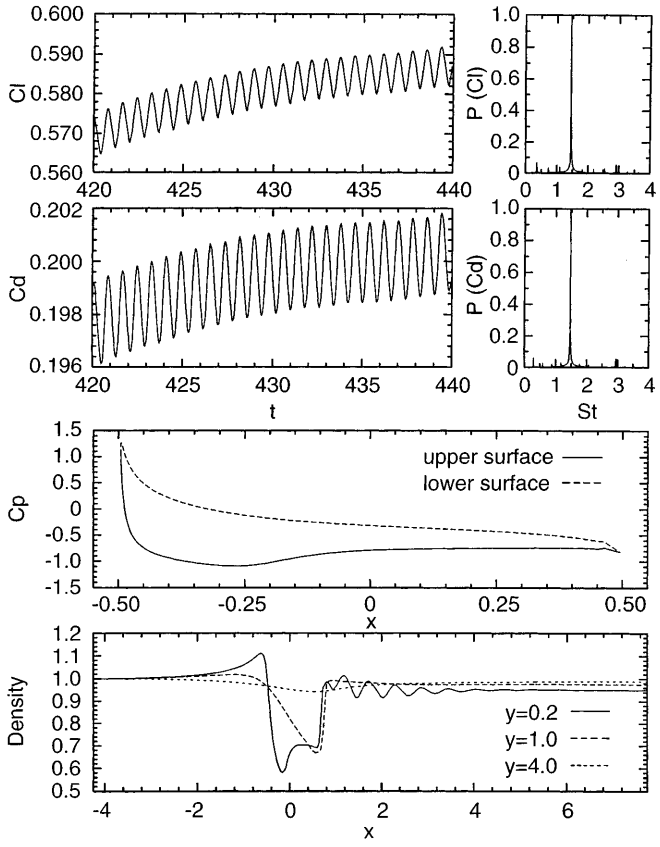

Fig. 28. Mach = 0.85, Re = 10,000, $\alpha = 8^\circ$, $H = 12$ flow past a *NACA*0012 airfoil: time histories of the lift and drag coefficients, their power spectra, the C_p distribution on the airfoil surface and the stream-wise variation of the density at various vertical locations corresponding to the peak value of the lift coefficient

value of the lift coefficient. These figures can be compared to Fig. 11 and 12 to study the effect of the location of lateral boundaries on the flow. Compared to the present computation, for the $H = 4.25$ case, there is a much more rapid acceleration of the flow near the nose of the airfoil causing a stronger expansion of the flow. This has a stabilizing effect on the shear layer leading to a reduced temporal activity in the wake. This can also be observed by comparing the amplitude of the lift and drag coefficients for the two cases. The Strouhal number for the present case is 1.4.

Figures 27 and 28 show the solution for $\alpha = 8^\circ$ while those for $\alpha = 10^\circ$ are shown in Figs. 29 and 30. Unlike the solutions for $H = 4.25$, all the computations for the present case result in temporally periodic solutions. The unsteadiness in the flow increases as the angle of attack of the airfoil, with respect to the incoming flow, increases. One can also observe that the shocks become stronger, the point of separation of the flow on the upper surface moves towards the leading edge as α increases. However, the Strouhal number for all the cases remains constant at approximately 1.4. The computations are repeated with different sets of initial conditions. In all the cases, the flow develops to the same temporally periodic state as described above. These observations are in sharp contrast to the ones made, earlier, for the $H = 4.25$ case.

Behr et al. (1995) have carried out a careful study to investigate the dependence of computed flow field on the location of the lateral boundaries on the incompressible flow past a circular cylinder. They observed that, for incompressible flows, bringing the lateral boundaries close to the cylinder results in an increase in the unsteadiness of the flow. This is manifested in the increased values of the Strouhal number and amplitude of lift coefficient. However, for the present study for transonic flows, it is seen that bringing the lateral boundaries close to the airfoil results in alleviation of the unsteadiness of the flow. Figure 31 summarizes the behavior of the various aerodynamic coefficients for the flows at various angles of attack for both locations of the lateral boundaries.

5 Concluding remarks

Results have been presented for the computation of unsteady, laminar, viscous transonic flows past a stationary airfoils at various angles of attack. The computations involve long-time integration of Navier-Stokes equations and demonstrate the robustness of the numerical scheme.

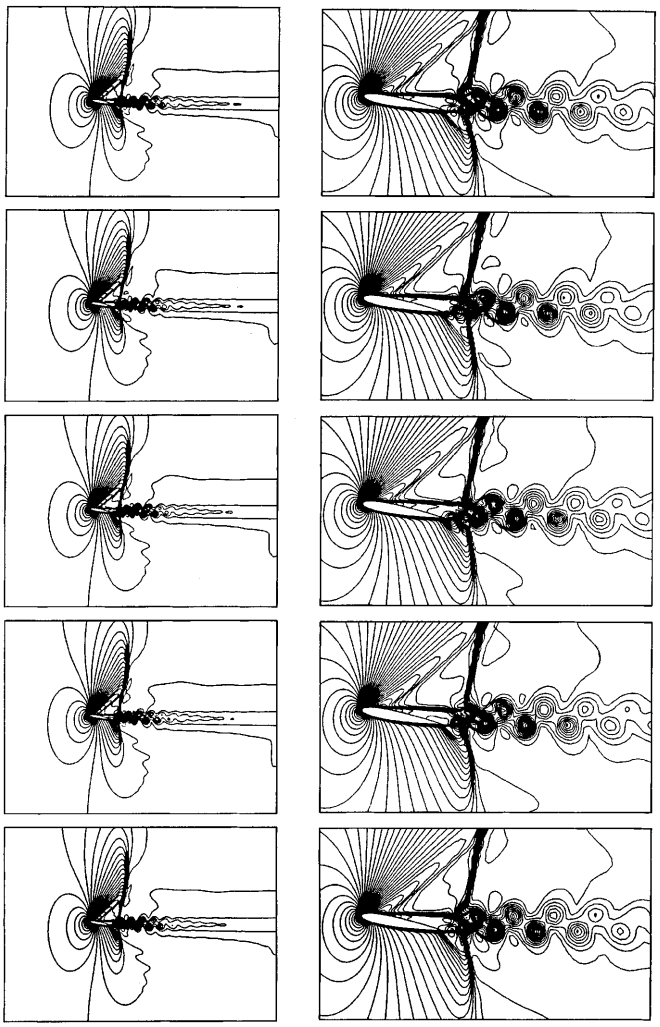

Fig. 29. Mach = 0.85, Re = 10,000, $\alpha = 10^\circ$, $H = 12$ flow past a *NACA*0012 airfoil: density field at five instants during one cycle of lift coefficient for the temporally periodic solution

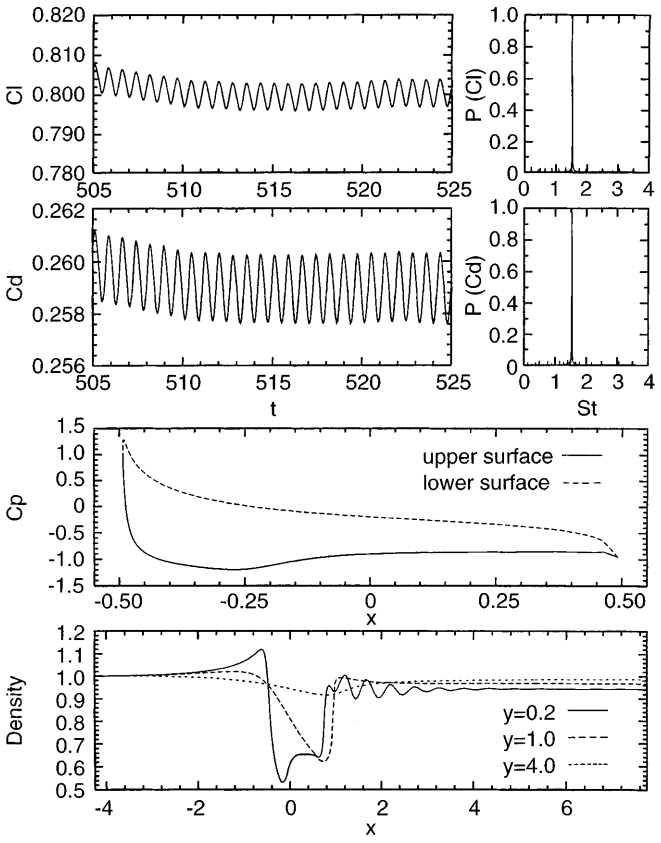

Fig. 30. Mach = 0.85, Re = 10,000, $\alpha = 10^\circ$, $H = 12$ flow past a *NACA*0012 airfoil: time histories of the lift and drag coefficients, their power spectra, the C_p distribution on the airfoil surface and the stream-wise variation of the density at various vertical locations corresponding to the peak value of the lift coefficient

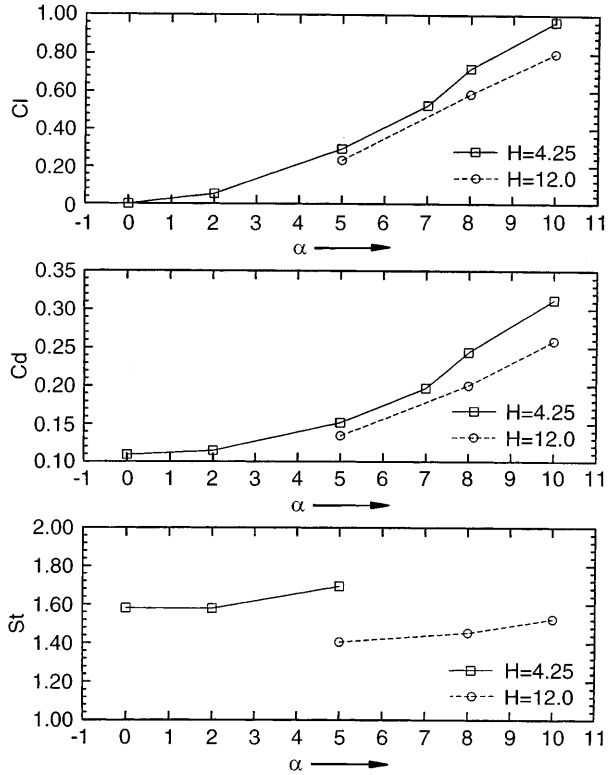

Fig. 31. Mach = 0.85, Re = 10,000 flow past a *NACA*0012 airfoil: Variation of the mean lift and drag coefficients and the Strouhal number with the angle of attack for both locations of the lateral boundaries. *H* is the distance between the lateral boundaries and the airfoil

Wherever available, good agreement has been observed with experimental and numerical results from other researchers. The results show interesting flow patterns and a complex interaction between the boundary/shear layers, shock/expansion waves and the lateral boundaries of the computational domain. For transonic flow past an airfoil at various angles of attack in a narrow channel/wind-tunnel one can observe solutions that are qualitatively different from each other. At a low angles of attack an unsteady wake is observed. At moderate angles of attack the interaction between the shock system and the lateral walls becomes significant and the temporal activity in the wake decreases and eventually disappears. At high angles of attack a reflection shock is formed. Hysteresis is observed at an angle of attack 8°. For the flow in a domain with the lateral boundaries located far away, the unsteadiness in the flow increases with an increase in the angle of attack.

References

Aliabadi SK (1994) Parallel Finite Element Computations in Aerospace Applications. PhD Thesis, Department of Aerospace Engineering and Mechanics, University of Minnesota

Aliabadi SK, Tezduyar TE (1993) Space-time finite element computation of compressible flows involving moving boundaries and interfaces. Comp. Meth. App. Mech. Eng. 107:209–224

Aliabadi SK, Tezduyar TE (1995) Parallel fluid dynamics computations in aerospace applications. Int. J. Num. Meth. Fluids 21

Aliabadi SK, Ray SE, Tezduyar TE (1993) SUPG finite element computation of compressible flows with the entropy and conservation variables formulations. Comput. Mech. 11:300–312

Allegre J, Raffin M, Lengrand JC (1987) Experimental flow-fields around *NACA* 0012 airfoils located in subsonic and supersonic rarefied air streams. In: Bristeau MO, Glowinski R, Periaux J, Viviand H, (eds) Numerical Simulation of Compressible Navier-Stokes Flows, volume 18 of Notes on Numerical Fluid Mechanics. Vieweg, Wiesbaden

Bassi F, Grasso F, Savini M (1988) A local multigrid strategy for viscous transonic flows around airfoils. In: Michel Deville, (ed), Proceedings of the Seventh GAMM-Conference on Numerical Methods in Fluid Mechanics, volume 20 of Notes on Numercial Fluid Mechanics, pp. 17–24. Vieweg, Wiesbaden

Behr M, Hastreiter D, Mittal S, Tezuyar TE (1995) Incompressible flow past a circular cylinder: Dependence of the computed flow field on the location of the lateral boundaries. Comp. Meth. Appl. Mech. Eng. 123:309–316

Boivin S, Fortin M (1993) A new artificial viscosity method for compressible viscous flow simulations by FEM. Int. J. Comput Fluid Dynam. 1:25–41

Bristeau MO, Pironneau O, Glowinski R, Periaux J, Perrier P, Poirier G (1985) On the numerical solution of nonlinear problems in fluid dynamics by least squares and finite element methods (II). Application to transonic flow simulations. Comp. Meth. Appl. Mech. Eng. 51:363–394

Bristeau MO, Glowinski R, Periaux J, Viviand H (1987) Presentation of problems and discussion of results. In: Bristeau MO, Glowinski R, Periaux J, Viviand H, (eds), Numerical Simulation of Compressible Navier-Stokes Flows, volume 18 of Notes on Numerical Fluid Mechanics, pp. 1–40. Vieweg, Wiesbaden

Bristeau MO, Glowinski R, Periaux J, Viviand H (1988) GAMM-workshop: Numercial simulation of compressible Navier-Stokes flows; Presentation of problems and discussion of results. In: Michel Deville, (ed), Proceedings of the Seventh GAMM-Conference on Numercial Methods in Fluid Mechanics, volume 20 of Notes on Numercial Fluid Mechanics, pp. 442–450. Vieweg, Wiesbaden

Dortmann K (1989) Computation of viscous unsteady compressible flow about airfoils. In: Dwoyer DL, Hussaini MY, Voigt RG, editors, 11th International Conference on Numerical Methods in Fluid Dynamics, Lecture Notes in Physics 323:230–234, Springer-Verlag

Gustafsson B, Sundstrom A (1978) Incompletely parabolic problems in fluid dynamics. SIAM J. Appl. Math. 35:343–357

Haase W (1987) Solutions of the Navier-Stokes equations for sub- and supersonic flows in rarefied gases. In: Bristeau MO, Glowinski R, Periaux J, Viviand H, (eds), Numerical Simulation of Compressible Navier-Stokes Flows, volume 18 of Notes on Numerical Fluid Mechanics. Vieweg, Wiesbaden

Hughes TJR, Brooks AN (1979) A multi-diensional upwind scheme with no crosswind diffusion. In: Hughes TJR, (ed), Finite Element Methods for Convection Dominated Flows, AMD-Vol. 34, pp. 19–35. ASME, New York

Hughes TJR, Mallet M (1986) A new finite element formulation for computational fluid dynamics: IV. A discontinuity-capturing operator for multidimensional advective-diffusive systems. Comp. Meth. Appl. Mech. Eng. 58:329–339

Hughes TJR, Tezduyar TE (1984) Fiinte element methods for first-order hyperbolic systems with particular emphasis on the compressible Euler equations. Comp. Meth. Appl. Mech. Eng. 45:217–284

Jameson A, Schmidt W (1985) Some recent developments in numerical methods for transonic flows. Comp. Meth. Appl. Mech. Eng. 51:467–493

Johan Z (1992) Data Parallel Finite Element Techniques for Large-Scale Computational Fluid Dynamics. PhD thesis, Department of Mechanical Engineering, Stanford University

Karanth D, Rankin GW, Sridhar K (1995) Computational study of flow past a cylinder with combined in-line and transverse oscillation. Comput. Mech. 16:1–10
Le Beau GJ (1990) The finite element computation of compressible flows. Master's thesis, Aerospace Engineering, University of Minnesota
Le Beau GJ, Tezduyar TE (1991) Finite element computation of compressible flows with the SUPG formulation. In: Dhaubhadel MN, Engelman MS, Reddy JN, (eds), Adv Finite Element Anal. Fluid Dynamics, FED-Vol. 123, pp. 21–27, New York ASME
Lohner R, Morgan K, Zienkiewicz OC (1985) An adaptive finite element procedure for compressible high speed flows. Comp. Meth. Appl. Mech. Eng. 51:441–465
Mittal S (1998) Finite element computation of unsteady viscous comprssible flows. To appear in Comp. Meth. Appl. Mech. Eng.
Mittal S, Tezduyar TE (1992) A finite element study of incompressible flows past oscillating cylinders and airfoils. Int. J. Num. Meth. Fluids 15:1073–1118
Mittal S, Tezduyar TE (1994) Massively parallel finite element computation of incompressible flows involving luid-body interactions. Comp. Meth. Appl. Mech. Eng. 112:253–282
Mittal S, Tezduyar TE (1995) Parallel finite element simulation of 3D incompressible flows: Fluid-structure interactions. Int. J. Num. Meth. Fluids 21:933–953
Muller B, Rizzi R (1988) Navier-Stokes solution for transonic flow over wings. In Michel Deville, editor, Proceedings of the Seventh GAMM-Conference on Numerical Methods in Fluid Mechanics, volume 20 of Notes on Numerical Fluid Mechanics, pp. 247–255. Vieweg, Wiesbaden
Oliger J, Sundstrom A (1978) Theoretical and practical aspects of some initial boundary value problems in fluid dynamics. SIAM J. Appl. Math. 35:419–446
Peraire J, Peiro J, Morgan K (1993) Finite element multigrid solution of Euler flows past installed aero-engines. Comp. Mech. 11:433–451
Saad Y, Schultz M (1986) GMRES: A generalized minimal residual algorithm for solving nonsymmetric linear systems. SIAM J. Scientif. Stat. Comput. 7:856–869
Sarkis M, Cia XC, Farhat C (1996) Variable degree Schwarz methods for implicit solution of unsteady compressible Navier-Stokes equations on unstructured meshes. Technical Report 96–48, Institute for Computer Applications in Science and Engineering, NASA Langley Research Center
Shapiro AH (1958) The Dynamics and Thermodynamics of Compressible Fluid Flows. John Wiley and Sons, New York
Tezduyar TE, Hughes TJR (1982) Development of time-accurate finite element techniques for first-order hyperbolic systems with particular emphasis on the compressible Euler equations. Report prepared under NASA-Ames University Consortium Interchange, No. NCA2-OR745-104
Tezduyar TE, Hughes TJR (1983) Finite element formulations for convection dominated flows with particular emphasis on the compressible Euler equations. In: Proceedings of AIAA 21st Aerospace Sciences Meeting, AIAA Paper 83–0125, Reno, Neveda
Tezduyar T, Aliabadi S, Behr M, Johnson A, Kalro V, Litke M (1996) Flow simulation and high performance computing. Computat. Mech. 18:397–412